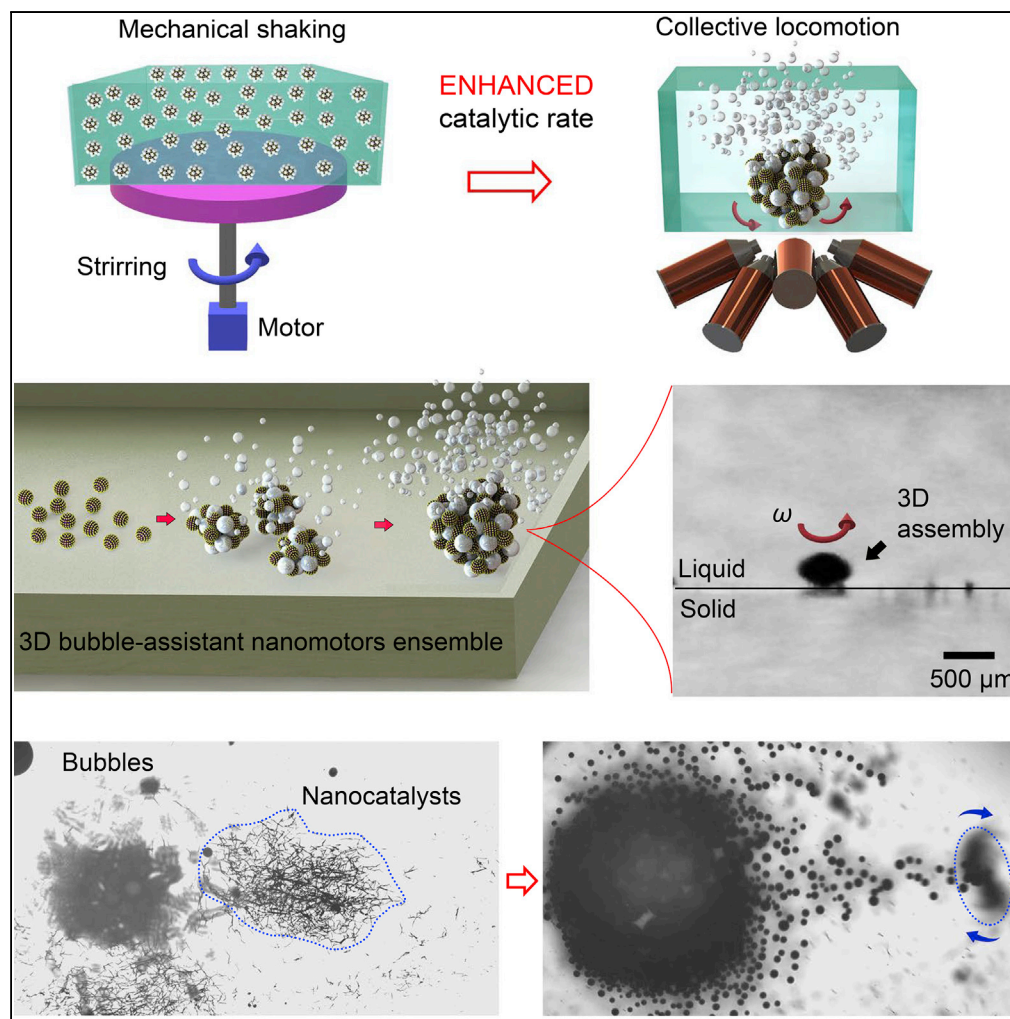


Article

Bubble-Assisted Three-Dimensional Ensemble of Nanomotors for Improved Catalytic Performance



Ben Wang,
Fengtong Ji,
Jiangfan Yu,
Lidong Yang,
Qianqian Wang, Li
Zhang

lizhang@mae.cuhk.edu.hk

HIGHLIGHTS

Bubbles convert the conventional 2D swarming behavior into 3D

Bubbles improve the collective motion velocity of nanomotors

Assembly and disassembly of the 3D bubbles-cross-linked nanoagents are realized

We verified the magnetic gathering of nanocatalysts enhanced the catalytic activity

Wang et al., iScience 19, 760–771
September 27, 2019 © 2019
The Author(s).
<https://doi.org/10.1016/j.isci.2019.08.026>

Article

Bubble-Assisted Three-Dimensional Ensemble of Nanomotors for Improved Catalytic Performance

Ben Wang,¹ Fengtong Ji,¹ Jiangfan Yu,¹ Lidong Yang,¹ Qianqian Wang,¹ and Li Zhang^{1,2,3,4,*}**SUMMARY**

Combining catalysts with active colloidal matter could keep catalysts from aggregating, a major problem in chemical reactions. We report a kind of ensemble of bubble-cross-linked magnetic colloidal swarming nanomotors (B-MCS) with enhanced catalytic activity because of the local increase of the nanocatalyst concentration and three-dimensional (3D) fluid convection. Compared with the two-dimensional swarming collective without bubbles, the integral rotation was boosted because of the dynamic dewetting and increased slip length caused by the continuously ejected tiny bubbles. The bubbles cross-link the nanocatalysts and form stack along the vertical axis, generating the 3D network-like B-MCS ensemble with high dynamic stability and low drag resistance. The generated B-MCS ensemble exhibits controllable locomotion performance when applying a rotating magnetic field. Benefiting from locally increased catalyst concentration, good mobility, and 3D fluidic convection, the B-MCS ensemble offers a promising approach to heterogeneous catalysis.

INTRODUCTION

Noble metal nanocrystals have been extensively investigated for achieving high efficiency and yield among organic catalysis (Chen et al., 2019; Dhakshinamoorthy et al., 2018; Jing et al., 2018; Stratakis and Garcia, 2012; B. Wang et al., 2018; Q. Wang et al., 2018; Liu et al., 2019). Owing to the high surface energy, the nanometer-scale catalysts tend to aggregate during the reaction, resulting in catalyst deactivation and difficulties for recycling. Therefore, researchers have employed a variety of strategies to maintain the segregation of noble metal nanoparticles by introducing extra cushion building blocks, such as on the surface of graphene oxide and metal-organic frameworks (Shang et al., 2014; Jiang et al., 2011; Gu et al., 2011; Zhang et al., 2014) and locking the noble metal nanoparticles inside micro-to-nano cavities for avoiding aggregation (Wang et al., 2011; Dhakshinamoorthy and Garcia, 2012; Wu et al., 2012). Composite nanomaterials with well-designed structures and components have attracted enormous attention in recent years to realize either the integrated properties of each ingredients or synergistically enhanced performances for organic synthesis via noble metal catalysis with enhanced product yield and cycle life (Deng et al., 2010; Ge et al., 2008; Yue et al., 2017). Although the stability and the recyclability of the noble nanoparticles have been improved, these kinds of particles systems still rely on the diffusion of the solutes and therefore reach the bottleneck for further improvement of catalytic efficiency, such as harvesting high-quality desired product, cost-saving from reduction of the usage amount of the noble metal, and the recyclability with magnetic collection

Combination of the catalysis and the active colloidal matter offers a new strategy for overcoming the bottleneck and improving the catalytic performance. Micro-/nanomotors have attracted wide interests for decades owing to their controlled motion capability generated from the conversion of various kinds of energy sources into mechanical energy (Chen et al., 2018; Kim et al., 2018; Wang et al., 2015, 2017; Wang and Pumera, 2015; Zhang et al., 2019). The self-propelled micro-/nanomotors are fuel dependent that required the chemical energy and biochemical energy derived from the surrounding environment for autonomous navigation. Although lots of the self-propelled micro-/nanomotors have been developed, particular attention was paid to the structural design of the micro-/nanomotors with the integration of the catalysts, such as noble metals and enzymes, in an asymmetric manner, so as to generate directional propulsion of the micro-/nanomotors (Gallino et al., 2018; Maric et al., 2018; Abdelmohsen et al., 2016; Patiño et al., 2018). The design and fabrication of self-propelled micro-/nanomotors with powerful and directional motion have been well demonstrated in previous studies (Sanchez et al., 2011; Solovev et al., 2010a, 2010b; Mei et al., 2008). Other micro-/nanomotors, which are powered by various external stimuli like magnetic, electric, light, and ultrasonic fields, possess the main merits of the remote actuation and steering. The

¹Department of Mechanical and Automation Engineering, The Chinese University of Hong Kong, Hong Kong, China

²Chow Yuk Ho Technology Centre for Innovative Medicine, The Chinese University of Hong Kong, Hong Kong, China

³T Stone Robotics Institute, The Chinese University of Hong Kong, Hong Kong, China

⁴Lead Contact

*Correspondence: lizhang@mae.cuhk.edu.hk
<https://doi.org/10.1016/j.isci.2019.08.026>



propulsion and navigation of individual micro-/nanorobots supplied with various kinds of energies have been extensively investigated during the past two decades. Different from the actuation of the individual micro-/nanorobots, and the independent propulsion of multi-agents, the swarming motion control of a cluster of tiny agents can perform integral and reconfigurable transportation of the micro-/nanoagents with ultra-low agent loss during the motion by many external stimuli (Chen et al., 2017; Yu et al., 2017a, 2017b, 2018a, 2018b; Wang et al., 2018a, 2018b; Ahmed et al., 2017; Ibele et al., 2009; Lin et al., 2017; Manjare et al., 2015; Hong et al., 2010; Deng et al., 2018; Solovev et al., 2010a, 2010b; 2013; Mou et al., 2019; Yigit et al., 2019; Zhou et al., 2018; Wang et al., 2018a, 2018b). Magnetic-field-controlled swarming of micro-/nanorobots offered an efficient strategy for the directed actuation and steering of a cluster of nanoagents. In our recent works (Yu et al., 2018a, 2018b; Wang et al., 2018a, 2018b), we developed a novel strategy to integrally transport a cluster of micro-/nanoagents as a 2D collective for the delivery purpose with remote magnetic field control. However, attributed to the requirement of force balance between the magnetic attraction for maintaining the swarming pattern and the fluidic drag effect for the integral translational motion, the efficiency of the simple magnetic actuation to form the magnetic microswarm and move it as a 2D dynamic collective is very limited. Moreover, with the increasing dose of the nanoagents, the area of the 2D pattern increases and the attraction effect to the outermost nanoagents will be weakened, causing the unstable of the collective. The drawbacks may hinder the motion and delivery efficiency of the micro-/nanoagents to the targeted location.

In this work, we developed a novel 3D ensemble consisting of a large number of bubble-cross-linked Fe_3O_4 @PDA-Au nanomotors, which showed ultra-high catalytic performance and mobility. The bubbles generated from the surface gold nanocrystals of the nanocatalysts play an important role in and benefit both the catalytic performance and the motion. First, the surface bubbles cross-link the building blocks of the bubble-cross-linked magnetic colloidal swarming nanomotors (B-MCS) and form a stack along the vertical axis to form a 3D ensemble, and they decrease the density of the B-MCS ensemble and increase its buoyancy. Second, the surface bubbles of nanocatalysts can significantly decrease the drag during the rotational and translational actuation of the B-MCS in fluid. Third, the escaped bubbles increase the fluid convection surrounding the B-MCS. Fourth, the bubbles enhance the interaction among the nanocatalysts inside the B-MCS ensemble via the interfacial tension. Fifth, the bubble-assistant collective locomotion enhances the catalytic performance of the nanocatalysts in three dimensions. As the bubble-assistant propulsion of individual micro-/nanomotors have been extensively explored in the past, this work gives a novel example of the bubble-accelerated motion of the collective behavior. Moreover, most of the previous swarm motions are two-dimensional (2D) planar assembly of the micro-/nanoagents with quite limited delivery dose. This work demonstrated that the micro-/nanoagents can be furtherly stacked along the vertical axis and generate a three-dimensional (3D) ensemble. Furthermore, the excellent mobility and 3D liquid convection make the B-MCS easily conduct an effective on-the-fly catalysis at the pre-assigned location with high spatial-temporal precision. The work is of potential industrial significance to enhance the catalytic efficiency and shorten the catalytic time during organic synthesis.

RESULTS

The multifunctional mesoporous nanocatalysts compose of, from inside to outside, a core of nonporous polydopamine (PDA)-protected magnetite microspheres (diameter = 250 nm) and a layer of dense and active gold nanoparticles (see Figures S1 and S2). Transmission electron microscopy (TEM) images reveal that the PDA layer shows a thickness of 5 nm, and the as-prepared Au nanocrystals show a uniform size of 4 nm (Figures 1A and S2). As reported previously, gold nanoparticles with an average size of 3.4 nm exhibit an optimized catalytic activity (Lin et al., 2013). The Energy Dispersive Spectrometer (EDS) mapping of the magnetic nanocatalysts verified the uniform elemental distributions of Fe, O, and Au (see Figure S3). X-ray photoelectron spectroscopy (XPS) spectra in Figure S4 verified the gold, iron, and other ingredients in the nanocatalysts.

The prepared nanocomposites can serve as a typical catalyst for various catalytic reactions. Here we use the catalytic synthesis of 4-aminophenol (4-AP) from 4-nitrophenol (4-NP) as an example. 4-AP is an important industrial chemical that is widely used in the drug discovery, as hair dyes, camera developers, and anti-aging agents in rubbers, with a rapidly increasing demand every year (Ai et al., 2019). The catalytic mechanism is systematically shown in Figure S5. Under the existence of the nanocatalysts, the sodium borohydride reacts with water quickly and generates the reductive BH_4^- and hydrogen gas. Traditional catalytic reactions generally apply the mechanical stirring process to homogenize the nanocatalysts within the solution to ensure sufficient contact and rapid diffusion, as schematically shown in Figure 1B. Here our proposed

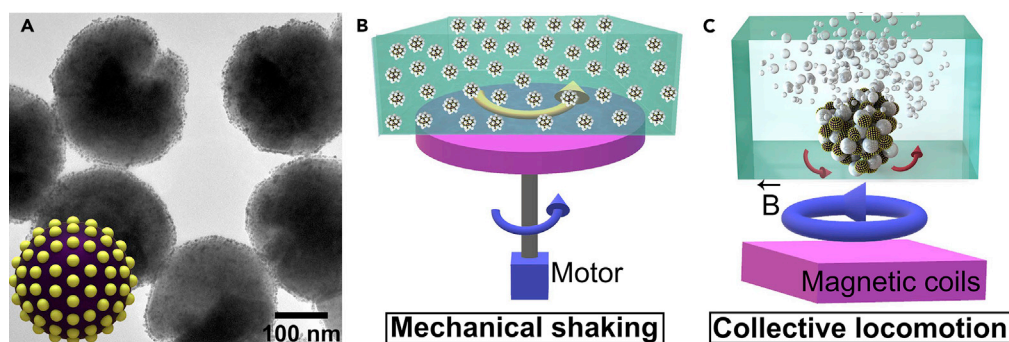


Figure 1. Schematics of the Conventional Catalysis and B-MCS Ensemble-Based Catalysis

(A) TEM image of Fe₃O₄@PDA-Au nanocatalysts. Inset is the structural model of the nanocatalyst.

(B) Schematic showing the conventional catalysis with violent mechanical stirring.

(C) Schematic showing the heterogeneous catalysis with the magnetic ensemble of bubble-cross-linked nanocatalysts (Video S1).

strategy uses the external magnetic field to assemble the nanocatalysts into 3D bubble-cross-linked ensemble (Figure 1C). The catalytic performance of the nanocatalysts in the two kinds of modes are studied. Figure 2A shows the experimental setups for performing the mechanical shaking and magnetic collective motion. While 20 μ L of 1 mg/mL nanocatalysts were added into the solutions, the catalytic reactions were monitored with UV-vis spectrometer. The gradual decrease of the absorption peak of the 4-NP solution at 400 nm indicates the gradual reduction of 4-NP to 4-AP. After 30 min of catalysis, the peak of the 4-NP for the B-MCS based catalysis nearly disappeared (Figure 2D) and the solution became colorless (Figure 2B). As for the catalysis process under violent shaking, the peak of the 4-NP shows a slight decrease (Figure 2C) and the color of the solution remains unchanged (Figure 2B). At this time point (30 min), the concentration of 4-NP in the solution with the catalytic B-MCS ensemble is only 22% of the concentration of 4-NP with violent shaking, indicating a much higher conversion ratio of the catalysis caused by B-MCS. The absorbances at 400 nm were recorded with different nanocatalysts concentrations as the time elapsed as shown in Figure 2E. The peaks gradually decrease and reach a steady stage finally. The increase of the nanocatalysts concentrations resulted in smaller steady absorbance. Surprisingly, the steady absorbance with a nanocatalyst concentration of 100 μ g/mL under the violent shaking still showed a higher value compared with the steady absorbance with a nanocatalysts concentration of 20 μ g/mL under the proposed B-MCS motion of the ensemble (see green curve and blue curve in Figure 2E). To evaluate the catalytic efficiency quantitatively, the pseudo-first order rate constants (k) at room temperature under the two kinds of catalytic modes were calculated via the slope of $\ln(C_t/C_0)$ (C_t and C_0 represent the concentrations of 4-NP at time t and 0 min) in Figure 2F. The rate constant under the B-MCS ensemble is six times higher than that under the violent shaking condition with evenly dispersed colloids in solution.

The magnetic field-triggered gathering of the bubbles-infused nanocatalysts is demonstrated in Figure 3. The magnetic colloidal swarm collective, as the control group in this work, was generated from the gathering of the nanocatalysts using a rotating magnetic field without the addition of sodium borohydride as schematically illustrated in Figure 3A. The B-MCS ensemble was generated from the gathering of the nanocatalysts under catalytic bubble reaction using a rotating magnetic field as schematically illustrated in Figure 3C. The side views of the control group and B-MCS in Figures 3B and 3D suggested that the configuration without bubbles is a 2D pattern, whereas the configuration of a B-MCS is a 3D pattern. The bubbles cross-link the nanocatalysts and form a stack along the z axis, generating the 3D B-MCS ensemble. The vertical axis stacking of the nanoagents significantly minimizes the spreading area than that of the conventional swarming process (Figures 3B and 3D), making the maximum dose of the swarming nanoagents larger than that of the conventional colloid swarm. Figure 3E gives the successive snapshots of the assembly process with both the variation of the nanocatalysts and the bubbles (field strength is 5 mT, input frequency is 6 Hz). As indicated by the blue dotted line, the nanocatalysts show a relatively uniform distribution in an elliptical area at the beginning. The inset shows the detail of the dispersed nanocatalysts with random chain-like structures due to the remanence of the material. After a rotating magnetic field was applied, the nanocatalysts quickly formed several small ensembles (Figures 3C and inset in 3E). As the time elapses, these rotating micro-ensembles successively merged with their neighbors and finally formed a

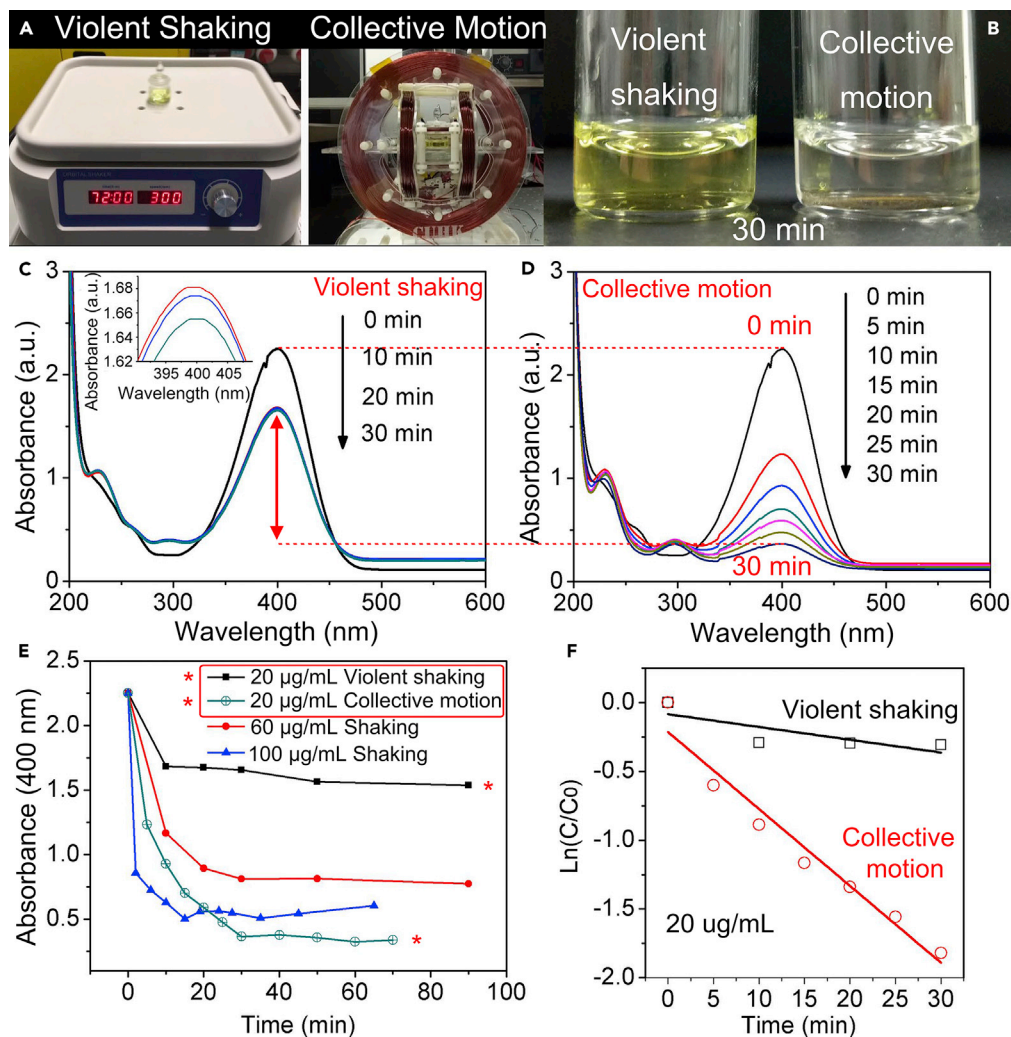


Figure 2. Comparison of Catalytic Performance under Violent Shaking and Magnetic Field Controlled Collective Motion

(A) Setups of the two kinds of catalytic modes.

(B) Optical image shows the solution before and after 30 min of catalysis under the two modes.

(C) UV-vis spectra of catalytic reduction of 4-nitrophenol to 4-aminophenol with 20 µg/mL of the nanocomposites as catalyst under the mechanical violent shaking mode.

(D) UV-vis spectra of catalytic reduction of 4-nitrophenol to 4-aminophenol with 20 µg/mL of the nanocomposites as catalyst under the collective motion (B-MCS) mode.

(E) The absorbance at 400 nm at different time points with 20, 60, and 100 µg/mL of nanocatalysts under violent shaking mode and with 20 µg/mL nanocatalysts under the B-MCS mode.

(F) The relationship between $\ln(C_t/C_0)$ and the reaction time with fixed nanocatalyst concentration under the two modes. (The value of the slope reflects the catalytic rate of among an organic synthesis system.)

larger rotating ensemble with significantly increased amount of bubble ejection than the original dispersed state and the intermediate state with several small ensembles. The merging process of two small ensembles under the magnetic field are recorded in [Figure 3F](#). The two rotating nanocatalyst ensembles assembled and merged with each other to form a larger B-MCS ensemble spontaneously after orbiting each other for a few laps, which is caused by the attraction of the induced fluidic vortices. From the measurement of the blue dotted circles in [Figure 3E](#), the final formed ensemble possessed a higher particle density than that of the original state. It is noted that the bubble ejection after the assembly is much more violent than the original nanocatalysts with a dispersed state (see [Figure S6](#)), demonstrating the faster catalytic reaction kinetics of the nanocatalysts originated from the collective motion and fluid convection of the gathered

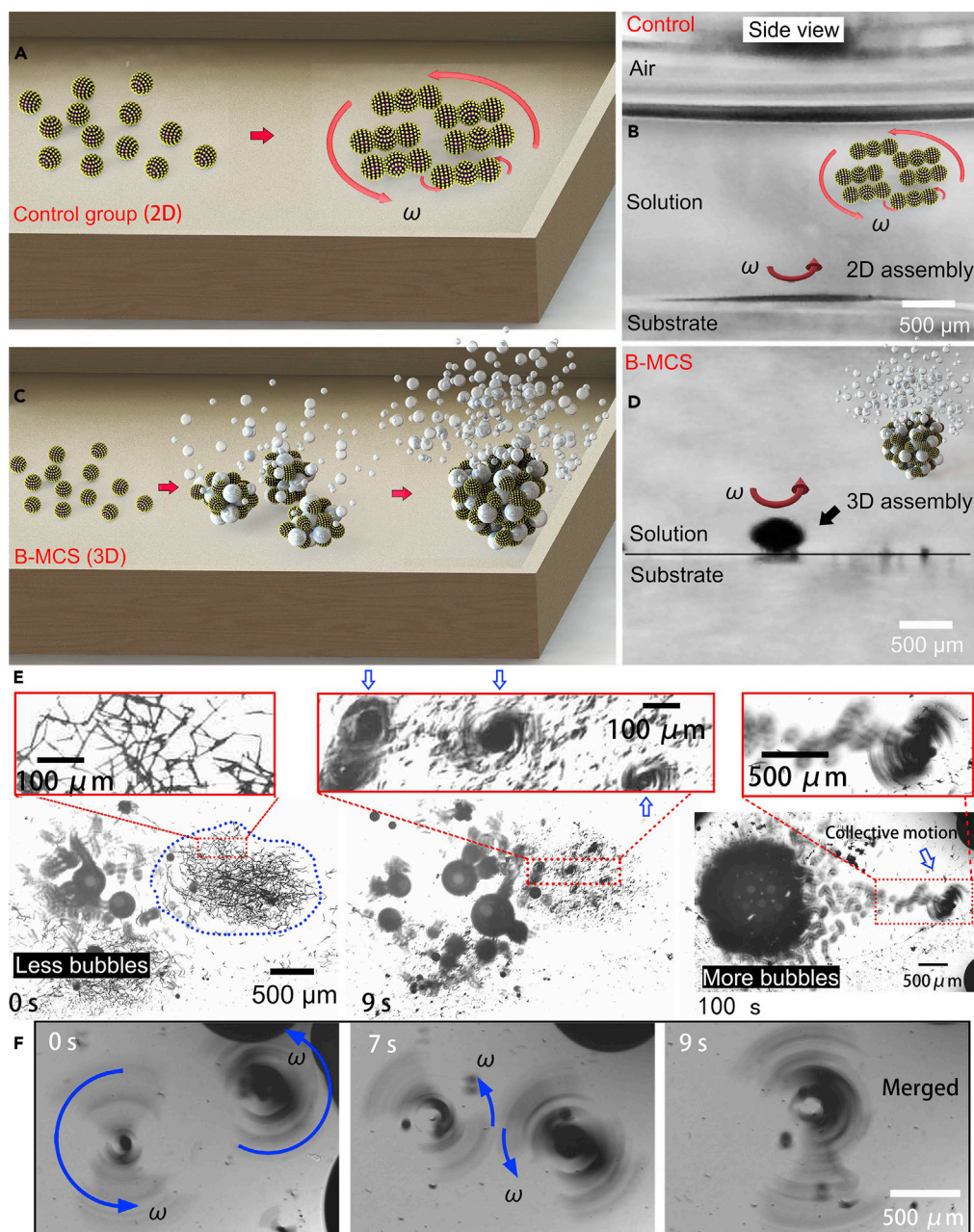


Figure 3. Dynamic Assembly of the Conventional 2D Colloidal Swarm and 3D B-MCS

(A) Schematic illustration of the assembly process of the nanocatalysts under rotating magnetic field in the 4-NP solution without addition of NaBH_4 .

(B) Side view of the 2D collective.

(C) Schematic illustration of the assembly process of the nanocatalysts under rotating magnetic field in the 4-NP solution with addition of NaBH_4 .

(D) Side view of the 3D B-MCS ensemble.

(E) Successive snapshots show the assembly process of the B-MCS under rotating magnetic field (5 mT, 6 Hz). The inset shows the enlarged view of the gradual shrunk pattern (Video S2).

(F) Spontaneous fusion process of the small gathered nanocatalysts.

nanocomposite pattern. The sodium borohydride is found to readily decompose on the surface of the nanocatalysts with hydrogen bubbles generated *in situ*. The gathering effect of nanocatalysts further accelerated the generation of the hydrogen gas. Inversely, the hydrogen bubbles not only facilitated the reduction of the 4-NP, but also improved the mobility of the collective behavior for enhanced planar motion and the diffusion of the solutes. In addition to the magnetic assembly of the nanocatalysts, the disassembly of an ensemble of the nanocatalysts into small micro-clusters after catalytic usage can be also realized, as shown in Figure S7 with a dynamic magnetic field.

Apart from the assembly of the B-MCS ensemble, the rotational and translational motions of the formed B-MCS were also studied. The rotational velocity (ω) of the 2D collective without bubbles is strongly related to the applied magnetic field frequency, and the increase of the dose of the building blocks will affect the integral rotating of the collective (Yu et al., 2017a, 2017b). Figure 4A gives the comparison of the rotation of the control group (without bubbles) and the B-MCS with the same magnetic field parameters (5 mT, 6 Hz). The B-MCS shows a higher apparent rotational revolution velocity with bubbles escaped from the pattern (indicated by the blue arrows in Figure 4A). The insets in Figure 4A show the schematics of the building blocks of the collectives without and with bubbles. As for the B-MCS, the building block contains not only the nanocatalyst but also the surface dynamic and ceaseless bubbles. Figure 4B gives the quantitative comparison of the apparent rotational velocities of the control group and B-MCS with different magnetic field frequencies. The rotational velocity of B-MCS shows a positive linear relationship with the magnetic field frequency. Compared with the velocities in the control group, as plotted by the red curves in Figure 4B, the rotational velocities of the B-MCS are significantly higher.

The accelerated rotating velocity is attributed to the surface dewetting effect by bubbles. The slip length is elongated. The generated bubbles, on the one hand, lowered the average volume density of the dynamic pattern. On the other hand, the generated bubble among the B-MCS ensembles dewet the particles surface to form the Cassie-Baxter wetting state (Wang et al., 2015, 2019a, 2019b; Lee and Kim, 2011; Cassie and Baxter, 1994; Jin et al., 2018) by converting the solid-liquid-solid interface into the solid-gas-solid interface and thus largely reduced the friction force between the nanocatalysts and the substrate. Likewise, on the other directions, the interface between the nanocatalysts and the solution was altered from the solid-liquid interface to solid-air-liquid interface, which also contributed to the spatial drag reduction. Liquid slip on the solid surface is critical to characterize the drag between the liquid and solid interface. As for the Newtonian fluid, the linear velocity profile around the solid phase will not vanish at the solid-liquid interface. The extrapolation depth into the solid (δ) to get a vanishing of the velocity is called slip length (Cottin-Bizonne et al., 2003). A larger slip length facilitates and promotes the drag reduction ability of the surface. As for the control group without bubbles, the nanocatalysts are completely wetted and form Wenzel state (Wenzel, 1936) as shown in Figure 4C. As for the B-MCS schematically shown in Figure 4D, the nanocatalysts stay in a dewetting state, which is called Cassie-Baxter state.

For the composite wetting state with both solid-liquid interface and gas-liquid interface, the slip length in these two states shows the following relationship with the fraction of the gas phase (Φ_g) (Lee et al., 2008).

$$\delta \sim L / \sqrt{1 - \Phi_g} \quad (\text{Equation 1})$$

where L is the pitch distance of the surface rough nanostructures. For the complete dewetting by the gas bubbles, the slip length shows the linear positive relationship with the thickness of the gas layer (b) (Choi and Kim, 2006).

$$\delta = b(\mu_l / \mu_a - 1) \quad (\text{Equation 2})$$

where μ_l and μ_a represent the viscosities of liquid and air, respectively. Equation 1 suggested that the gas bubble trapped on the nanocatalysts can increase the slip length. If one neglects the gold nanobumps on the magnetic particle surface, an air film can be obtained. It increases with the increasing bubble volume. The trapped bubbles volumes will reach a saturated state and the redundant gas will escape from the surface, achieving a dynamic equilibrium. Equation 2 suggested that both the increase of the thickness of the air film and the viscosity of the liquid phase can cause the increase of the slip length. As indicated in Figure 4C, the nanocatalysts collective without catalytic bubbles show a large velocity gradient perpendicular to the nanocomposite surface. The fraction of the gas phase (Φ_g) is zero, which makes the slip length extremely low according to Equation 1. Although the nanocatalysts cluster continuously ejects bubbles

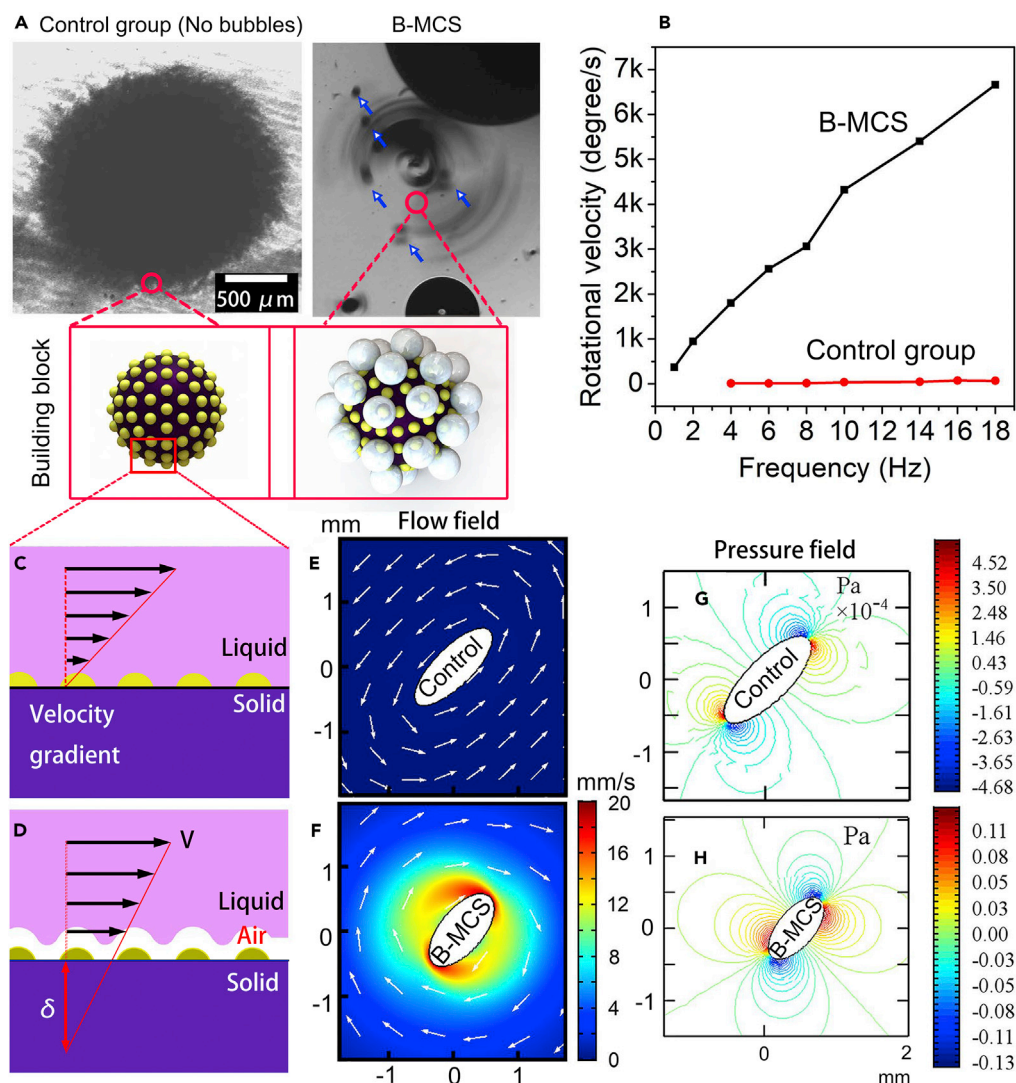


Figure 4. Rotational Motion of the B-MCS Ensemble

(A) Microscopic images show the control group and B-MCS (5 mT, 6 Hz). The inset at the bottom shows the schematics of the building blocks of the control group and B-MCS.

(B) The relationship between the rotational velocity and magnetic field frequency for the B-MCS and control group (field strength is 10 mT).

(C and D) Schematics of the slip length of the collective locomotion caused by bubble-infused liquid slip mechanism. (C) As for the control group, the velocity gradient near the nanocatalysts surface is significant with a small slip length. (D) As for the B-MCS, the velocity gradient near the nanocatalysts surface is quite small because of the dewetting, and the slip length in this case is large.

(E and F) Simulation results of the flow field of the control group and B-MCS. The higher flow field indicates the higher liquid convection.

(G and H) Simulation results of the pressure field of the control group and B-MCS. The higher pressure field indicates the higher disturbance.

outward, it will be wrapped with a dynamic gas film and the ϕ_g ($0 < \phi_g < 1$) is much larger than the former case, causing the increase of the slip length and the decrease of the drag. The amount of the dynamic gas bubbles can also affect the slip length in the form of gas film thickness according to Equation 2. The gas film will result in a larger slip length and smaller resistance. The drag reduction property of the bubble-cross-linked nanomotors were furtherly verified by the simulation results of the spatial flow field and pressure field. As shown in Figures 4E and 4F, the maximum value of liquid flow around the nanocatalysts is about $100 \mu\text{m/s}$ for the control group, whereas the flow reaches about $10,000 \mu\text{m/s}$ for the B-MCS, indicating a

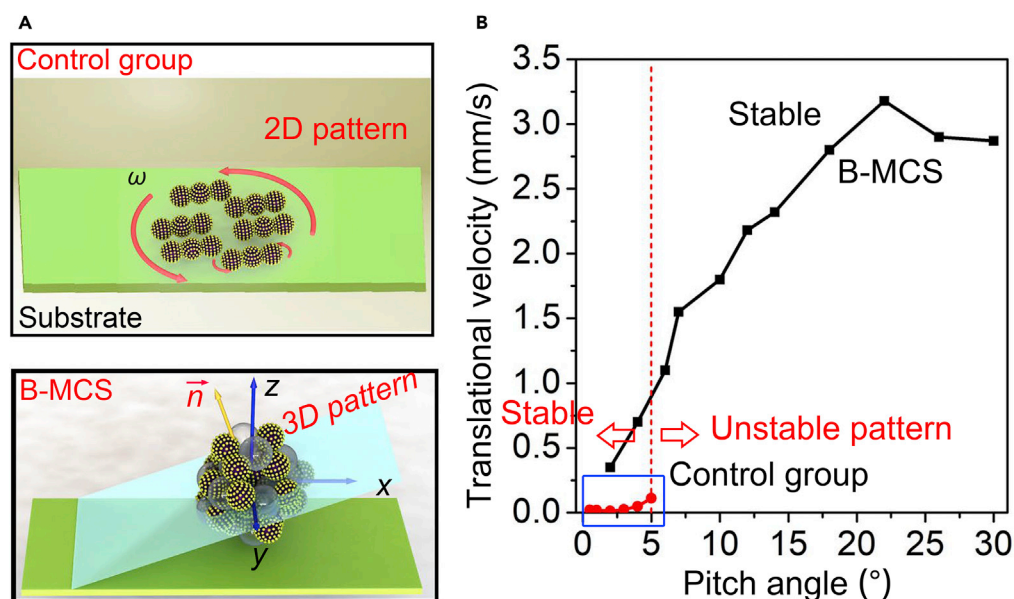


Figure 5. Translational Locomotion of the B-MCS Ensemble

(A) Schematic of the translational motion of the bubble-free collective and B-MCS ensembles with an applied pitch angle (Video S3).

(B) The relationship of the translational velocity and pitch angle for the B-MCS and the control group (field strength is 10 mT, input frequency is 15 Hz).

significantly improved fluid convection. Meanwhile, the maximum pressure generated by the B-MCS is about three orders of magnitude compared with that of the control group (Figures 4G and 4H). The simulation results suggested that the B-MCS cluster possessed an enhanced mobility and drag reduction properties and also contributed to the increase of the fluid convection.

The translational velocity of a swarm is mainly determined by the pitch angles, as schematically illustrated in Figures 5A and S8. The tilt of the swarm plane leads to the translational locomotion, and the direction is controllable by tuning the direction angle. Figure 5B gives the quantitative investigation of the translational velocities and pitch angles of the B-MCS and the control group with the same magnetic field parameters (field strength is 10 mT and frequency is 15 Hz) and dose of the nanocatalysts (8 μ L, 1 mg/mL). The translational velocity of a B-MCS increases rapidly with the increase of the pitch angle, until the velocity reaches its maximum of about 3 mm/s (Figure 5B). Compared with the control group as plotted by the red curves in Figure 5B, the translational velocities of the B-MCS are significantly larger with different pitch angles. Video S3 shows the translational motion of the B-MCS and the control group along a channel under the same field frequency of 6 Hz. The trajectory of the B-MCS can also be controlled in a programmable fashion as shown in Figures S9 and S10. More importantly, the 2D swarm pattern without bubbles became unstable while the pitch angle was larger than 5°, making the reachable translational velocity quite limited and only up to about 0.1 mm/s as shown in Figure 5B. The reason is that the typical 2D planar pattern formed in the control group is mainly stabilized by the fluidic trapping force. It cannot adapt the large tilt angle of the swarm plane and would cause instability of the dynamic patterns, which may cause the collapse of the pattern. As for the B-MCS with 3D configuration, the pitch angle is unrestricted because the nanocatalysts are cross-linked by the interfacial tension of microbubbles in both the x-y plane and z axis, making the collective inclinable and stable. From the comparison in Figure 5B, the reachable translational velocity of B-MCS is about 30 times larger than that of the control group, indicating its merit in spatial navigation. The simulation results of the control group and B-MCS are specifically illustrated in Figures S11–S14, indicating an enhanced flow field and pressure field generated by the B-MCS locomotion. As a result, the spatially enhanced catalytic performance was achieved and illustrated in Figure S15.

The enhanced catalytic performance can be interpreted from the two aspects. First, the cross-linking effect generated by the microbubbles causes the gathering and stacking of the nanocatalysts and forms locally increased concentration of the nanocatalysts, making the local catalysis effective. Second, B-MCS motion

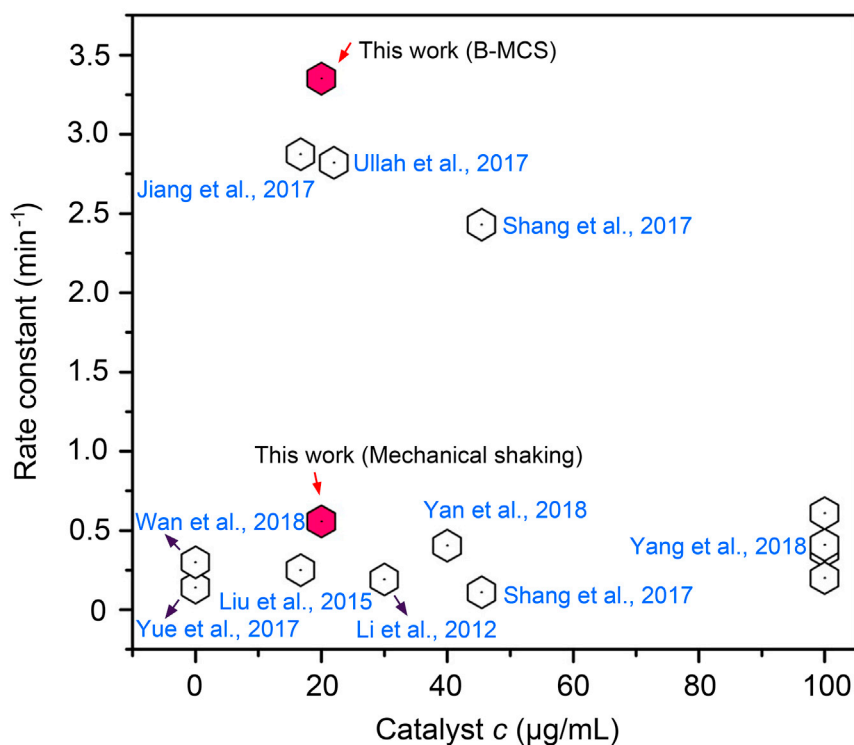


Figure 6. Comparison of the Rate Constant with the Current State-of-the-Art Nanocatalysts

The data are retrieved from the references (Jiang et al., 2017; Li et al., 2012; Liu et al., 2015; Shang et al., 2017; Ullah et al., 2017; Wan et al., 2018; Yan et al., 2018; Yang et al., 2018; Yue et al., 2017).

triggers the enhanced fluid convection in the 3D space. Specifically, the fluid convection at the x-y plane was promoted by the high-speed rotation of the B-MCS as indicated in Figure 4F. The fluid convection along the z axis was promoted by the continuous escape of the bubbles from the bottom B-MCS during the rotation. The combined effect of the increased local catalysts concentration and the promoted 3D fluid convection triggered the significant increase of the catalytic rate constant and the spatial catalytic performance. We furtherly compared the catalytic performance of our result with the current state-of-the-art works. As shown in Figure 6, the nanocatalysts with B-MCS motion show (highlighted in red) much better catalytic performances than the current state-of-the-art works using different kinds of catalysts. For the catalysis under violent shaking, the performance is in the normal range. The results suggested that the proposed strategy may show potential industrial significance by shortening the catalytic time and saving the usage of the noble metal catalysts during organic synthesis.

DISCUSSION

This work reports an efficient strategy to realize an enhanced catalytic activity than that of the violent stirring-based heterogeneous catalysis in a uniform manner. The improved catalytic performance is achieved by the magnetically controlled gathering and collective motion of the bubble-cross-linked nanocatalysts. Compared with the swarming collective without bubbles, the integral rotation was improved because of the dynamic dewetting and increased slip length caused by the ejected bubbles. The translational locomotion was also strikingly boosted because of the cross-linking ability of the internal bubbles among the nanocatalysts in z axis, which made the B-MCS three-dimensional and stable even under large pitch angles. The B-MCS can be navigated with the external magnetic field with programmable trajectory, and easily be actuated to designated location to perform rapid catalysis. Benefitting from the locally increased catalysts concentration and 3D promoted fluid convection, the catalytic activity of the B-MCS can achieve a constant rate of 3.4 min⁻¹ under a low nanocatalyst concentration of 20 µg/mL, exceeding the performance on the current state-of-the-art 4-NP and 4-AP catalytic systems. The proposed B-MCS shows its potential industrial impact on the enhanced catalytic efficiency, shortened catalytic time, cost-saving from reduction of the usage amount of the noble metal, and recycling property with magnetic collection.

Limitations of the Study

Although the improved catalytic performance is achieved in laboratory-scale vials, the strategy shows its limitation in the scale-up toward the real industrial applications. The Helmholtz coils setup generally possesses very limited working distance. To scale-up the bubbles assistant swarming catalytic system, the magnetic actuation system may require further improvement to increase the working distance. In addition, the enhanced collective motion of the B-MS-C ensemble is realized in the bubbles participated catalytic system; for the catalytic reactions without bubbles, the proposed strategy may not work.

METHODS

All methods can be found in the accompanying [Transparent Methods supplemental file](#).

SUPPLEMENTAL INFORMATION

Supplemental Information can be found online at <https://doi.org/10.1016/j.isci.2019.08.026>.

ACKNOWLEDGMENTS

This work was partially supported by the General Research Fund (GRF) from the Research Grants Council (RGC) of Hong Kong with Project Numbers 14203715 and 14218516, the ITF project funded by the HKSAR Innovation and Technology Commission (ITC) with Project Numbers MRP/036/18X and ITS/231/15. The authors thank Dongdong Jin and Shijie Wang for the discussion and revision of this work. B.W. would like to thank the financial support from the Impact Postdoctoral Fellowship Scheme from the Chinese University of Hong Kong.

AUTHOR CONTRIBUTIONS

B.W. and L.Z. designed the processing approach. B.W. conducted the experiments and wrote the manuscript with input from the other authors. L.Z. mentored the work and revised the manuscript. F.J. performed the simulation. B.W. and L.Y. performed the actuation control. J.Y. and Q.W. provided expertise and feedback.

DECLARATION OF INTERESTS

The authors declare no competing interests.

Received: June 20, 2019

Revised: August 3, 2019

Accepted: August 16, 2019

Published: September 27, 2019

REFERENCES

- Abdelmohsen, L.K.E.A., Nijemeisland, M., Pawar, G.M., Janssen, G.A., Nolte, R.J.M., van Hest, J.C.M., and Wilson, D.A. (2016). Dynamic loading and unloading of proteins in polymeric stomatocytes: formation of an enzyme-loaded supramolecular nanomotor. *ACS Nano* *10*, 2652–2660.
- Ahmed, D., Baasch, T., Blondel, N., Laubli, N., Dual, J., and Nelson, B.J. (2017). Neutrophil-inspired propulsion in a combined acoustic and magnetic field. *Nat. Commun.* *8*, 770.
- Ai, Y., Hu, Z., Liu, L., Zhou, J., Long, Y., Li, J., Ding, M., Sun, H., and Liang, Q. (2019). Magnetically hollow Pt nanocages with ultrathin walls as a highly integrated nanoreactor for catalytic transfer hydrogenation reaction. *Adv. Sci.* *6*, 1802132.
- Cassie, A., and Baxter, S. (1994). Wettability of porous surfaces. *Trans. Faraday Soc.* *40*, 546–561.
- Chen, M., Cai, F., Wang, C., Wang, Z., Meng, L., Li, F., Zhang, P., Liu, X., and Zheng, H. (2017). Observation of metal nanoparticles for acoustic manipulation. *Adv. Sci.* *4*, 1600447.
- Chen, T., Xu, Y., Guo, S., Wei, D., Peng, L., Guo, X., Xue, N., Zhu, Y., Chen, Z., Zhao, B., and Ding, W. (2019). Ternary heterostructural Pt/CNx/Ni as a supercatalyst for oxygen reduction. *iScience* *11*, 388–397.
- Chen, X.-Z., Jang, B., Ahmed, D., Hu, C., Marco, C.D., Hoop, M., Mushtaq, F., Nelson, B.J., and Pane, S. (2018). Small-scale machines driven by external power sources. *Adv. Mater.* *30*, 1705061.
- Choi, C.-H., and Kim, C.-J. (2006). Large slip of aqueous liquid flow over a nanoengineered superhydrophobic surface. *Phys. Rev. Lett.* *96*, 066001.
- Cottin-Bizonne, C., Barrat, J.-L., Bocquet, L., and Charlaix, E. (2003). Low-friction flows of liquid at nanopatterned interfaces. *Nat. Mater.* *2*, 237–240.
- Deng, Y.H., Cai, Y., Sun, Z.K., Liu, J., Liu, C., Wei, J., Li, W., Liu, C., Wang, Y., and Zhao, D.Y. (2010). Multifunctional mesoporous composite microspheres with well-designed nanostructure: a highly integrated catalyst system. *J. Am. Chem. Soc.* *132*, 8466–8473.
- Deng, Z., Mou, F., Tang, S., Xu, L., Luo, M., and Guan, J. (2018). Swarming and collective migration of micromotors under near infrared light. *Appl. Mater. Today* *13*, 45–53.
- Dhakshinamoorthy, A., and Garcia, H. (2012). Catalysis by metal nanoparticles embedded on metal-organic frameworks. *Chem. Soc. Rev.* *41*, 5262–5284.
- Dhakshinamoorthy, A., Li, Z., and Garcia, H. (2018). Catalysis and photocatalysis by metal organic frameworks. *Chem. Rev.* *47*, 8134–8172.
- Gallino, G., Gallaire, F., Lauga, E., and Michelin, S. (2018). Physics of bubble-propelled microrockets. *Adv. Funct. Mater.* *28*, 1800686.

- Ge, J.P., Zhang, Q., Zhang, T.R., and Yin, Y.D. (2008). Core–satellite nanocomposite catalysts protected by a porous silica shell: controllable reactivity, high stability, and magnetic recyclability. *Angew. Chem. Int. Ed.* **47**, 8924–8928.
- Gu, X., Lu, Z.-H., Jiang, H.-L., Akita, T., and Xu, Q. (2011). Synergistic catalysis of metal–organic framework-immobilized Au–Pd nanoparticles in dehydrogenation of formic acid for chemical hydrogen storage. *J. Am. Chem. Soc.* **133**, 11822–11825.
- Hong, Y.Y., Diaz, M., Cordova-Figueroa, U.M., and Sen, A. (2010). Light-driven titanium-dioxide-based reversible microfireworks and micromotor/micropump systems. *Adv. Funct. Mater.* **20**, 1568–1576.
- Ibele, M., Mallouk, T.E., and Sen, A. (2009). Schooling behavior of light-powered autonomous micromotors in water. *Angew. Chem. Int. Ed.* **48**, 3308–3312.
- Jiang, H.-L., Akita, T., Ishida, T., Haruta, M., and Xu, Q. (2011). Synergistic catalysis of Au@Ag core–shell nanoparticles stabilized on metal–organic framework. *J. Am. Chem. Soc.* **133**, 1304–1306.
- Jiang, Y.-F., Yuan, C.-Z., Xie, X., Zhou, X., Jiang, N., Wang, X., Imran, M., and Xu, A.-W. (2017). A novel magnetically recoverable Ni–CeO₂-x/Pd nanocatalyst with superior catalytic performance for hydrogenation of styrene and 4-nitrophenol. *ACS Appl. Mater. Interfaces* **9**, 9756–9762.
- Jin, J., Zhao, X., Du, Y., Ding, M., Xiang, C., Yan, N., Jia, C., Han, Z., and Sun, L. (2018). Nanostructured three-dimensional percolative channels for separation of oil-in-water emulsions. *iScience* **6**, 289–298.
- Jing, K., Wang, Y., Liang, Q., and Sun, H. (2018). Pd–CuFe catalyst for transfer hydrogenation of nitriles: controllable selectivity to primary amines and secondary amines. *iScience* **8**, 61–73.
- Kim, K., Guo, J., Liang, Z., and Fan, D. (2018). Artificial micro/nanomachines for bioapplications: biochemical delivery and diagnostic sensing. *Adv. Funct. Mater.* **28**, 1705867.
- Lee, C., and Kim, C.-J. (2011). Underwater restoration and retention of gases on superhydrophobic surfaces for drag reduction. *Phys. Rev. Lett.* **106**, 014502.
- Lee, C., Choi, C.-H., and Kim, C.-J. (2008). Structured surfaces for a giant liquid slip. *Phys. Rev. Lett.* **101**, 064501.
- Li, J., Liu, C.-Y., and Liu, Y. (2012). Au/graphene hydrogel: synthesis, characterization and its use for catalytic reduction of 4-nitrophenol. *J. Mater. Chem.* **22**, 8426–8430.
- Lin, C., Tao, K., Hua, D., Ma, Z., and Zhou, S. (2013). Size effect of gold nanoparticles in catalytic reduction of p-nitrophenol with NaBH₄. *Molecules* **18**, 12609–12620.
- Lin, Z.H., Si, T.Y., Wu, Z.G., Gao, C.Y., Lin, X.K., and He, Q. (2017). Light-activated active colloid ribbons. *Angew. Chem. Int. Ed.* **56**, 13517–13520.
- Liu, G.Q., Wang, D.A., Zhou, F., and Liu, W.M. (2015). Electrostatic self-assembly of au nanoparticles onto thermosensitive magnetic core-shell microgels for thermally tunable and magnetically recyclable catalysis. *Small* **11**, 2807.
- Liu, L., Liu, Y., Ai, Y., Li, J., Zhou, J., Fan, Z., Bao, H., Jiang, R., Hu, Z., Wang, J., et al. (2019). Surfactant-assisted cooperative self-assembly of nanoparticles into active nanostructures. *iScience* **11**, 272–293.
- Manjare, M., Yang, F.C., Qiao, R., and Zhao, Y.P. (2015). Marangoni flow induced collective motion of catalytic micromotors. *J. Phys. Chem. C* **119**, 28361–28367.
- Maric, T., Mayorga-Martinez, C.C., Khezri, B., Nasir, M.Z.M., Chia, X., and Pumera, M. (2018). Nanorobots constructed from nanoclay: using nature to create self-propelled autonomous nanomachines. *Adv. Funct. Mater.* **28**, 1802762.
- Mei, Y., Huang, G., Solovev, A.A., Urena, E.B., Monch, I., Ding, F., Reindl, T., Fu, R.K.Y., Chu, P.K., and Schmidt, O.G. (2008). Versatile approach for integrative and functionalized tubes by strain engineering of nanomembranes on polymers. *Adv. Mater.* **20**, 4085–4090.
- Mou, F., Zhang, J., Wu, Z., Du, S., Zhang, Z., Xu, L., and Guan, J. (2019). Phototactic flocking of photochemical micromotors. *iScience* **19**, 415–424.
- Patiño, T., Feiner-Gracia, N., Arqué, X., Miguel-López, A., Jannasch, A., Stumpp, T., Schäffer, E., Albertazzi, L., and Sánchez, S. (2018). Influence of enzyme quantity and distribution on the self-propulsion of non-janus urease-powered micromotors. *J. Am. Chem. Soc.* **140**, 7896–7903.
- Stratakis, M., and Garcia, H. (2012). Catalysis by supported gold nanoparticles: beyond aerobic oxidative processes. *Chem. Rev.* **112**, 4469–4506.
- Shang, L., Bian, T., Zhang, B., Zhang, D., Wu, L., Tung, C., Yin, Y., and Zhang, T. (2014). Graphene-supported ultrafine metal nanoparticles encapsulated by mesoporous silica: robust catalysts for oxidation and reduction reactions. *Angew. Chem. Int. Ed.* **53**, 250–254.
- Sanchez, S., Ananth, A.N., Fomin, V.M., Viehrig, M., and Schmidt, O.G. (2011). Superfast motion of catalytic microjet engines at physiological temperature. *J. Am. Chem. Soc.* **133**, 14860–14863.
- Shang, L., Liang, Y.H., Li, M.Z., Waterhouse, G.I.N., Tang, P., Ma, D., Wu, L.-Z., Tung, C.-H., and Zhang, T.R. (2017). “Naked” magnetically recyclable mesoporous Au–γ-Fe₂O₃ nanocrystal clusters: a highly integrated catalyst system. *Adv. Funct. Mater.* **27**, 1606215.
- Solovev, A.A., Mei, Y., and Schmidt, O.G. (2010a). Catalytic microstrider at the air–liquid interface. *Adv. Mater.* **2**, 4340–4344.
- Solovev, A.A., Sanchez, S., Pumera, M., Mei, Y.F., and Schmidt, O.G. (2010b). Magnetic control of tubular catalytic microbots for the transport, assembly, and delivery of micro-objects. *Adv. Funct. Mater.* **20**, 2430–2435.
- Solovev, A.A., Sanchez, S., and Schmidt, O.G. (2013). Collective behaviour of self-propelled catalytic micromotors. *Nanoscale* **5**, 1284–1293.
- Ullah, N., Imran, M., Liang, K., Yuan, C.-Z., Zeb, A., Jiang, N., Qazi, U.Y., Sahar, S., and Xu, A.-W. (2017). Highly dispersed ultra-small Pd nanoparticles on gadolinium hydroxide nanorods for efficient hydrogenation reactions. *Nanoscale* **9**, 13800–13807.
- Wan, L., Song, H.Y., Chen, X., Zhang, Y., Yue, Q., Pan, P.P., Su, J.C., Elzatahy, A.A., and Deng, Y.H. (2018). A magnetic-field guided interface coassembly approach to magnetic mesoporous silica nanochains for osteoclast-targeted inhibition and heterogeneous nanocatalysis. *Adv. Mater.* **30**, 1707515.
- Wang, B., Chan, K.F., Yu, J.F., Wang, Q.Q., Yang, L.D., Chiu, P.W.Y., and Zhang, L. (2018a). Reconfigurable swarms of ferromagnetic colloids for enhanced local hyperthermia. *Adv. Funct. Mater.* **28**, 1705701.
- Wang, Q., Zhang, C., Shi, L., Zeng, G., Zhang, H., Li, S., Wu, P., Zhang, Y., Fan, Y., Liu, G., et al. (2018b). Ultralow Pt catalyst for formaldehyde removal: the determinant role of support. *iScience* **9**, 487–501.
- Wang, B., Liang, W.X., Guo, Z.G., and Liu, W.M. (2015). Biomimetic super-lyophobic and super-lyophilic materials applied for oil/water separation: a new strategy beyond nature. *Chem. Soc. Rev.* **44**, 336–361.
- Wang, H., and Pumera, M. (2015). Fabrication of micro/nanoscale motors. *Chem. Rev.* **115**, 8704–8735.
- Wang, H., Potroz, M.G., Jackman, J.A., Khezri, B., Maric, T., Cho, N.-J., and Pumera, M. (2017). Bioinspired spiky micromotors based on sporopollenin exine capsules. *Adv. Funct. Mater.* **27**, 1702338.
- Wang, B., Chan, K.F., Ji, F.T., Wang, Q.Q., Chiu, P.W.Y., Guo, Z.G., and Zhang, L. (2019a). On-demand coalescence and splitting of liquid marbles and their bioapplications. *Adv. Sci.* **6**, 1802033.
- Wang, Q., Yang, L., Wang, B., Yu, E., Yu, J., and Zhang, L. (2019b). Collective behavior of reconfigurable magnetic droplets via dynamic self-assembly. *ACS Appl. Mater. Interfaces* **11**, 1630–1637.
- Wang, S.N., Zhang, M.C., and Zhang, W.Q. (2011). Yolk–shell catalyst of single Au nanoparticle encapsulated within hollow mesoporous silica microspheres. *ACS Catal.* **1**, 207–211.
- Wenzel, R.N. (1936). Resistance of solid surfaces to wetting by water. *Ind. Eng. Chem.* **28**, 988–994.
- Wu, S., Dzubiella, J., Kaiser, J., Drechsler, M., Guo, X.H., Ballauff, M., and Lu, Y. (2012). Thermosensitive Au-PNIPAA yolk–shell nanoparticles with tunable selectivity for catalysis. *Angew. Chem. Int. Ed.* **51**, 2229–2233.
- Yue, Q., Li, J.L., Zhang, Y., Cheng, X.W., Chen, X., Pan, P.P., Su, J.C., Elzatahy, A.A., Alghamdi, A., Deng, Y.H., and Zhao, D.Y. (2017). Plasmolysis-inspired nanoengineering of functional yolk–shell microspheres with magnetic core and mesoporous silica shell. *J. Am. Chem. Soc.* **139**, 15486–15493.

- Yu, J.F., Xu, T.T., Lu, Z.Y., Vong, C.I., and Zhang, L. (2017a). On-demand disassembly of paramagnetic nanoparticle chains for microbotic cargo delivery. *IEEE Trans. Robot.* **33**, 1213.
- Yu, J.F., Jin, D.D., and Zhang, L. (2017b). Mobile Magnetic Nanoparticle-Based Vortex for Targeted Cargo Delivery in Fluid. *IEEE Int. Conf. On Robotics and Automation (ICRA 2017) (IEEE)*, p. 6594.
- Yu, J.F., Wang, B., Du, X.Z., Wang, Q.Q., and Zhang, L. (2018a). Ultra-extensible ribbon-like magnetic microswarm. *Nat. Commun.* **9**, 3260.
- Yu, J.F., Yang, L.D., and Zhang, L. (2018b). Pattern generation and motion control of a vortex-like paramagnetic nanoparticle swarm. *Int. J. Robot. Res.* **37**, 912–930.
- Yan, R., Zhao, Y., Yang, H., Kang, X.-J., Wang, C., Wen, L.-L., and Lu, Z.-D. (2018). Ultrasmall Au nanoparticles embedded in 2D mixed-ligand metal–organic framework nanosheets exhibiting highly efficient and size-selective catalysis. *Adv. Funct. Mater.* **28**, 1802021.
- Yang, J., Yuan, M., Xu, D., Zhao, H., Zhu, Y.Y., Fan, M.Y., Zhang, F.W., and Dong, Z.P. (2018). Highly dispersed ultrafine palladium nanoparticles encapsulated in a triazinyl functionalized porous organic polymer as a highly efficient catalyst for transfer hydrogenation of aldehydes. *J. Mater. Chem. A*. **6**, 18242–18251.
- Yigit, B., Alapan, Y., and Sitti, M. (2019). Programmable collective behavior in dynamically self-assembled mobile microbotic swarms. *Adv. Sci.* **6**, 1801837.
- Zhang, W., Lu, G., Cui, C.L., Liu, Y.Y., Li, S.Z., Yan, W.J., Xing, C., Chi, Y.R., Yang, Y.H., and Huo, F.W. (2014). A family of metal-organic frameworks exhibiting size-selective catalysis with encapsulated noble-metal nanoparticles. *Adv. Mater.* **26**, 4056–4060.
- Zhang, Y., Yuan, K., and Zhang, L. (2019). Micro/nanomachines: from functionalization to sensing and removal. *Adv. Mater. Technol.* **4**, 1800636.
- Zhou, D., Gao, Y., Yang, J., Li, Y.C., Shao, G., Zhang, G., Li, T., and Li, L. (2018). Light-ultrasound driven collective “Firework” behavior of nanomotors. *Adv. Sci.* **5**, 1800122.

ISCI, Volume 19

Supplemental Information

**Bubble-Assisted Three-Dimensional
Ensemble of Nanomotors
for Improved Catalytic Performance**

Ben Wang, Fengtong Ji, Jiangfan Yu, Lidong Yang, Qianqian Wang, and Li Zhang

SUPPLEMENTAL INFORMATION

Bubble-assisted three-dimensional ensemble of nanomotors for improved catalytic performance

*Ben Wang^a, Fengtong Ji^a, Jiangfan Yu^a, Lidong Yang^a, Qianqian Wang^a, Li Zhang^{*a,b,c}*

^aDepartment of Mechanical and Automation Engineering, The Chinese University of Hong Kong, Hong Kong, China

^bChow Yuk Ho Technology Centre for Innovative Medicine, The Chinese University of Hong Kong, Hong Kong, China

^cT Stone Robotics Institute, The Chinese University of Hong Kong, Hong Kong, China

Correspondence and requests for materials should be addressed to L.Z. (email:

lizhang@mae.cuhk.edu.hk)

Supplemental Information includes:

Transparent Methods.

Figure S1. TEM images of Fe_3O_4 particles, Fe_3O_4 @PDA particles, and Fe_3O_4 @PDA-Au particles.

Figure S2. Adjustment of the amount and size of the Au NPs, and enlarged view shows the surface PDA layer and the uniform Au NPs.

Figure S3. STEM image of a Fe_3O_4 @PDA-Au particle and EDS maps of Fe, O and Au elements of the boxed region.

Figure S4. Integral and high-resolution XPS spectra.

Figure S5. Schematic illustration catalytic reduction of the 4-NP into 4-AP.

Figure S6. Optical images show the ejected bubbles (dynamic equilibrium state) before and after gathering of the nanocatalysts using rotational magnetic field.

Figure S7. Disassembly process of a cluster of nanocatalysts into lots of small clusters along with the increase of the coverage area of the nanocatalysts.

Figure S8. The locomotion of the B-MCS with programed trajectory.

Figure S9. The navigating B-MCS cut the bubbles around their trajectory.

Figure S10-S13. Simulation results of the pressure field and flow field among translational locomotion.

Figure S14. Spatial enhancement of the catalytic activity.

Video S1. Catalysis with fixed amount of nanocatalysts under two modes: violent shaking and collective locomotion.

Video S2. Magnetic field triggered gathering of nanocatalysts with increased bubble generation.

Video S3. Comparison of the navigation of the nanocatalysts collectives without bubbles and with bubbles assistance from addition of catalytic solution.

TRANSPARENT METHODS

Preparation of magnetite microspheres

The preparation of magnetite microspheres was conducted following the method described in the literature. (Deng et al., 2005) Briefly, 1.35 g of $\text{FeCl}_3 \cdot 6\text{H}_2\text{O}$ was dissolved in 40 mL of EG by vigorous stirring to form an orange clear solution. Next, 3.6 g of NaAc and 1.0 g of PEG (MW = 50 000) were added to the solution with ultrasound treatment for 30 min. Then, the mixture was sealed in a Teflon-lined stainless-steel autoclave and heated at 200 °C for 10 h, after which the autoclave was allowed to cool to room temperature. The black products were washed with ethanol and DI water for three times, respectively. The magnetic particles were finally stored in DI water with a concentration of 20 mg/mL for further usage.

Synthesis of Fe_3O_4 @PDA microspheres

100 mL 10 mM aqueous solution of tris(hydroxymethyl)aminomethane was prepared and the pH of the solution was adjusted to 8.5 to form Tri-HCl buffer. Then, 100 mg of Fe_3O_4 microspheres was dispersed in the buffer and the mixture was suffered with sonication for half an hour. 0.02 g of dopamine was added into the solution and the self-polymerization was processed for 5 h under continuous ultrasound treatment with ice-water bath. Afterward, the black product was collected by a magnet and washed with deionized water and ethanol for three times, respectively. The Fe_3O_4 @PDA microspheres were stored in DI water with a concentration of 5 mg/mL for further usage.

Synthesis of gold nanoparticles

The preparation of gold nanoparticles was conducted following the method described in the literature. (Jana et al., 2001; Choi et al., 2017) Briefly, 600 μL of 25 mM $\text{HAuCl}_4 \cdot 3\text{H}_2\text{O}$ solution and 600 μL of 25 mM sodium citrate were added into 58.8 mL DI water under magnetic stirring. After 10 min, 900 μL 0.2 M NaBH_4 solution was added into the solution, causing the color change from yellow to wine red. After another 15 min stirring, the solution was stored in dark and aged for 2h.

Synthesis of Fe₃O₄@PDA-Au nanocatalysts

10 mg of Fe₃O₄@PDA microspheres was dispersed in 50 mL of citrate buffer with pH = 3 and sonicated for 10 min to induce a surface positive charge of the microspheres. Then, the above-prepared Au colloid solution was poured into the Fe₃O₄@PDA microspheres suspension and the mixture was sonicated for 5 min. The product was collected by a magnet and washed with deionized water for three times. The Fe₃O₄@PDA-Au microspheres were stored in DI water with a concentration of 1 mg/mL for further usage.

Catalytic synthesis of 4-aminophenol (4-AP)

40 μ L of 4-NP (0.05 M) aqueous solution, 0.5 mL of fresh prepared NaBH₄ aqueous solution (0.1 M), and 2.5 mL of DI water were homogenized in a glass vessel with shaking. The solution was quickly subjected to UV-vis characterization and the obtained data was assigned to the reaction at t = 0 min. Then, certain amount of suspension of nanocatalysts was added into the vessel and the vessel was subjected with the two mode as specified in the maintext. The UV-vis spectra were taken every 3 min in the wavelength range of 200 ~ 600 nm to record the successive information of the reaction.

Characterization

TEM and STEM images were performed on a Tecnai F20 system (FEI, USA) and with an X-ray energy dispersive spectrometer (EDS) attachment for elementary mapping. The chemical composition of the as-prepared surfaces was investigated using X-ray photoelectron spectroscopy (XPS), which was conducted on an Escalab 250Xi electron spectrometer (Thermo Scientific, USA). The C 1s binding energy (284.6 eV) was used as the reference.

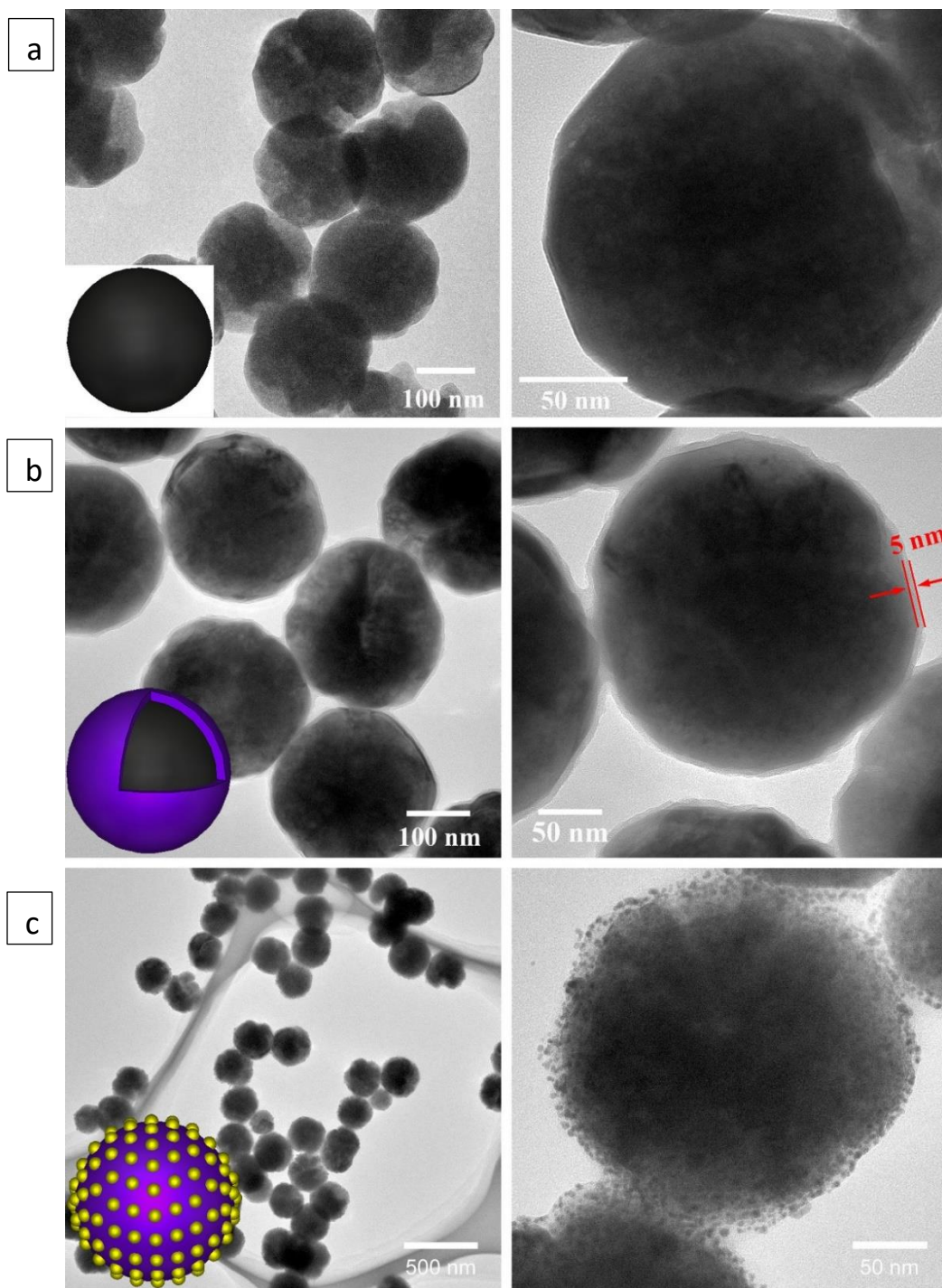


Figure S1. SEM images showing the fabrication process of the samples, Related to Figure 1. (a) TEM images of Fe₃O₄ particles. (b) TEM images of Fe₃O₄@PDA particles. (c) TEM images of Fe₃O₄@PDA-Au particles. Insets in (a), (b) and (c) are the structural models of Fe₃O₄, Fe₃O₄@PDA, and Fe₃O₄@PDA-Au particles.

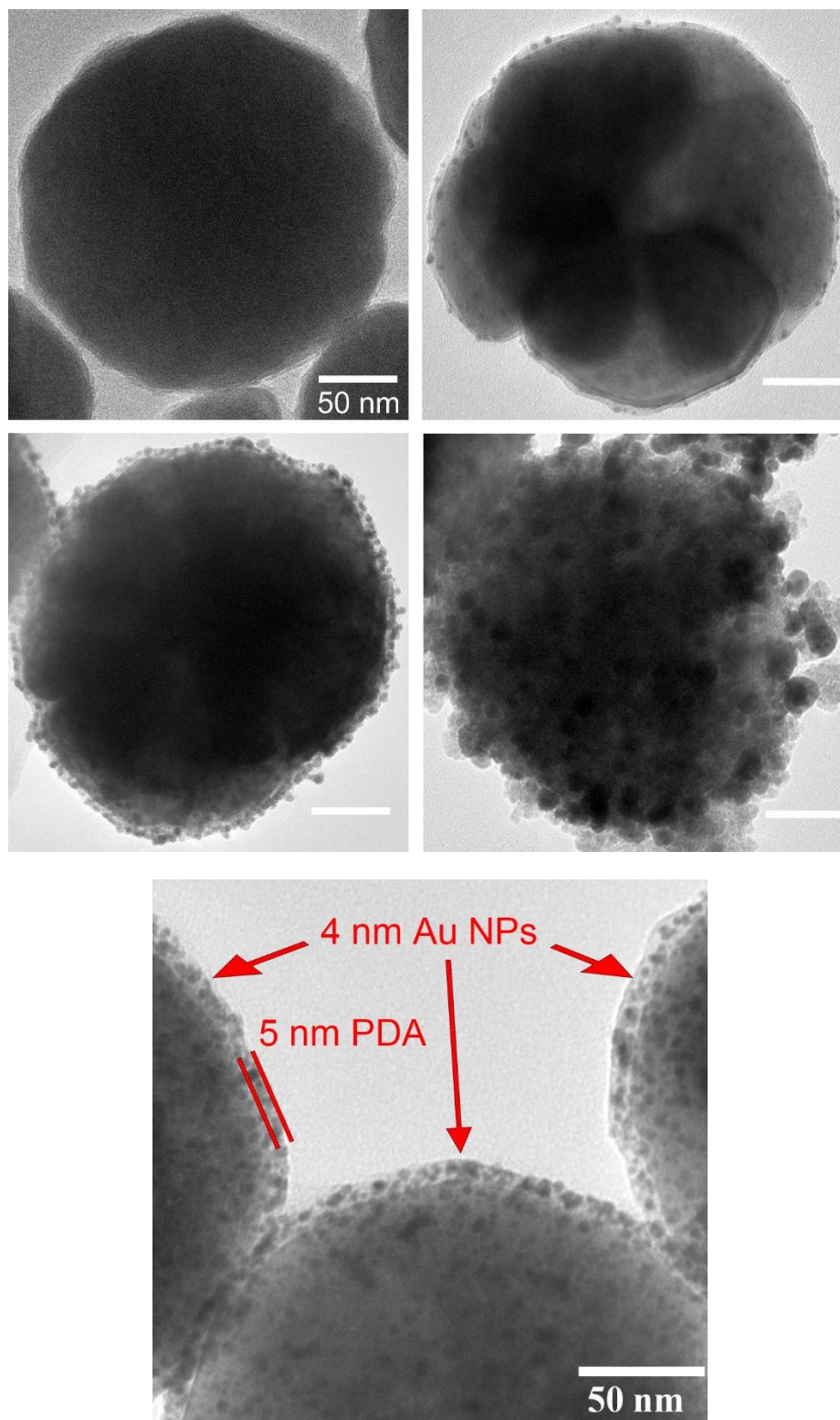


Figure S2 Adjustment of the amount of surface Au NPs and size of the Au NPs, Related to Figure 1.
Enlarged view shows the surface PDA layer and the uniform Au NPs.

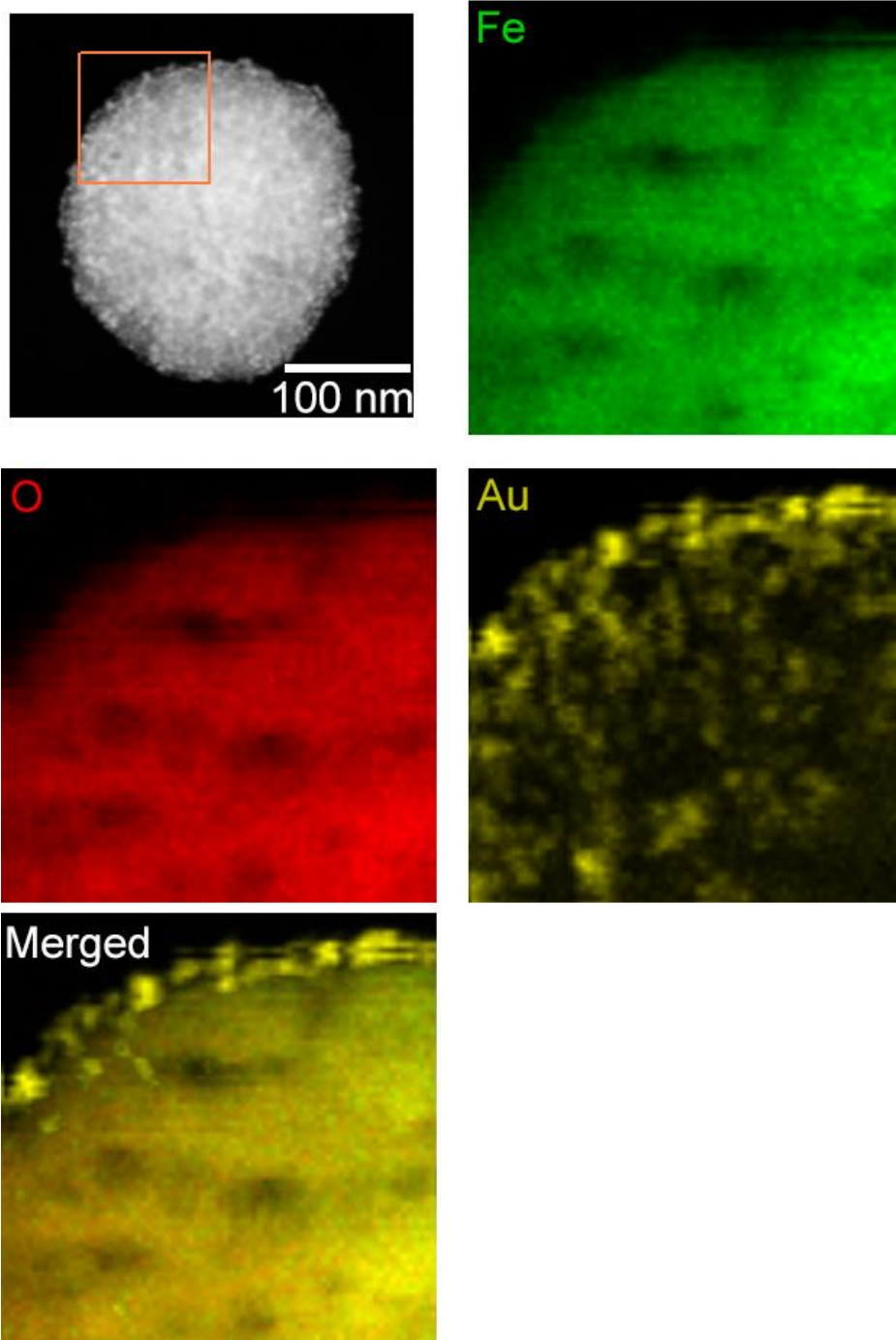


Figure S3 STEM image of a $\text{Fe}_3\text{O}_4@PDA\text{-Au}$ particle and EDS maps of Fe, O and Au elements of the boxed region, Related to Figure 1.

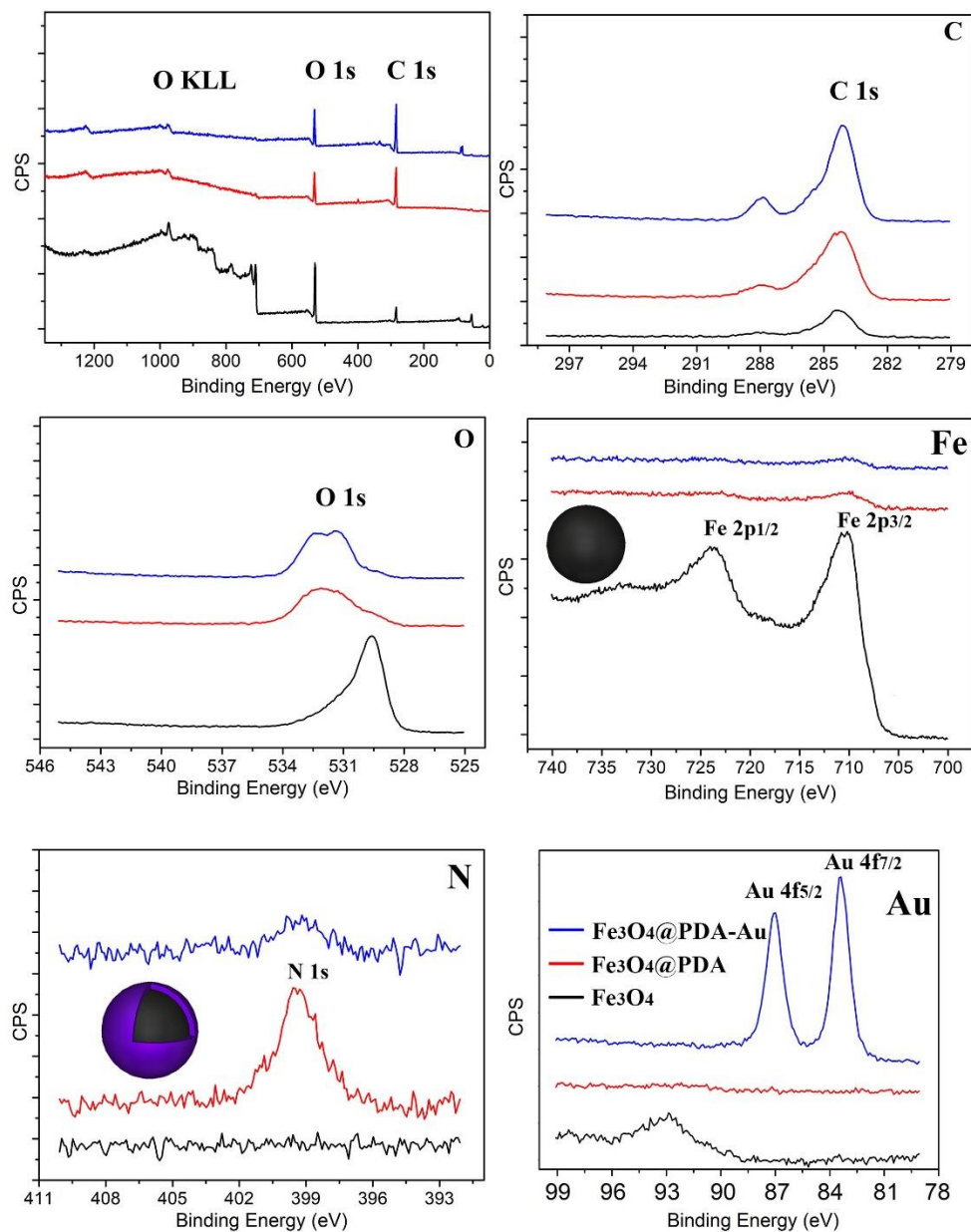


Figure S4 Integral and high-resolution XPS spectra of C 1s, O 1s, Fe 2p, N 1s and Au 4f of the Fe₃O₄ (black curve), Fe₃O₄@PDA (red curve), and Fe₃O₄@PDA-Au (blue curve) particles, Related to Figure 1.

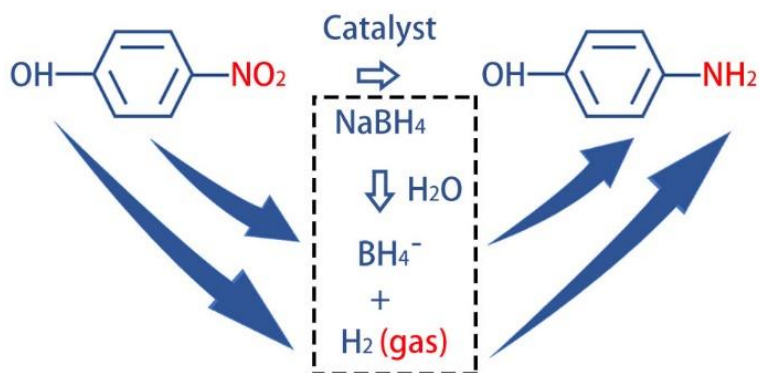


Figure S5 Schematic illustration catalytic reduction of the 4-NP into 4-AP by using the nanocatalysts under the existence of NaBH₄, Related to Figure 2.

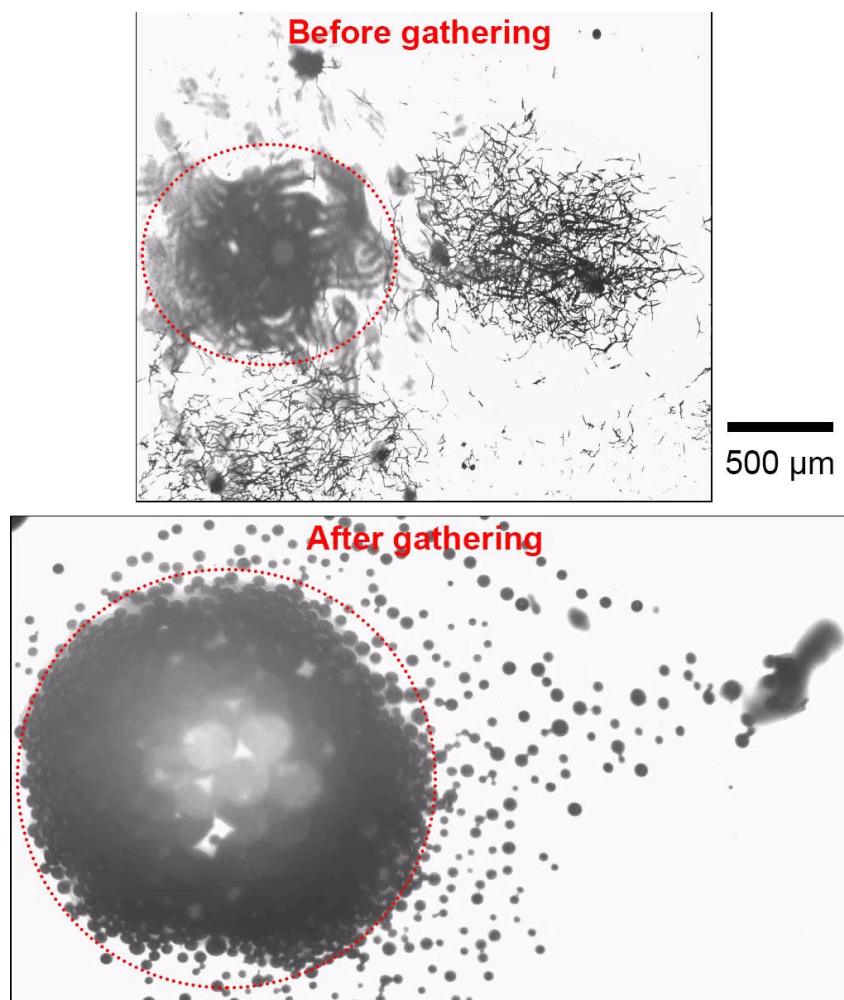


Figure S6 Optical images show the ejected bubbles (dynamic equilibrium state) before and after gathering of the nanocatalysts using rotational magnetic field, Related to Figure 3.

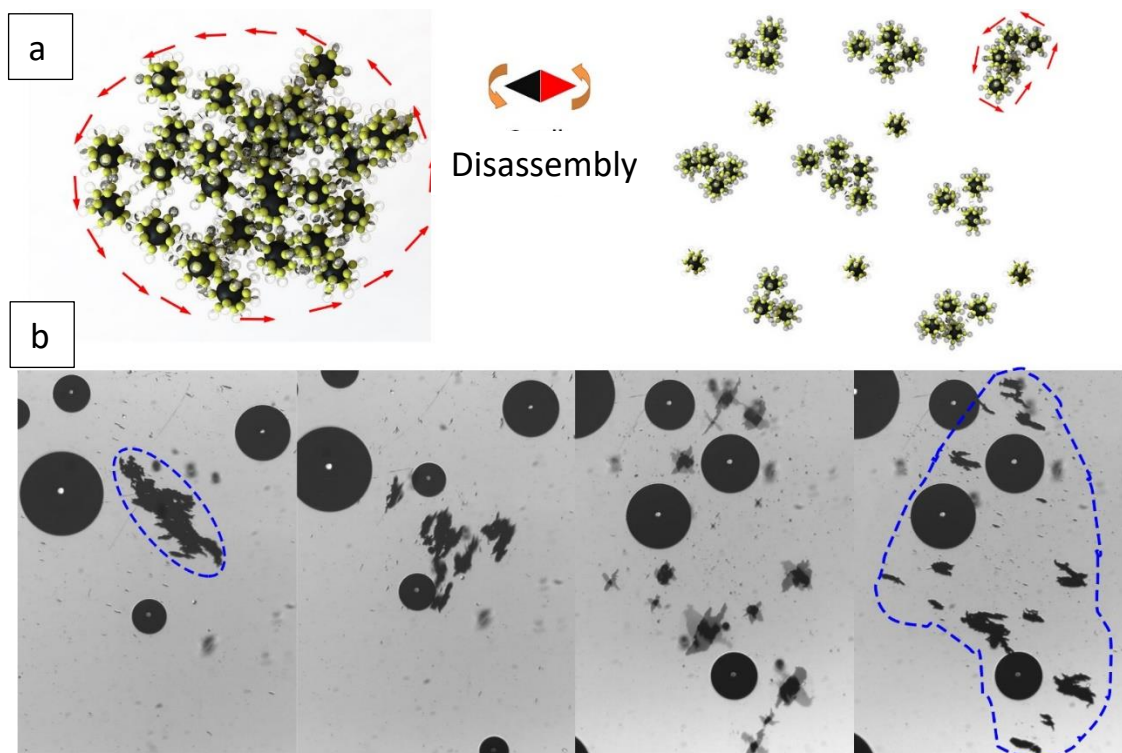


Figure S7 Disassembly of the gathered nanocatalysts. Related to Figure 3. (a) Schematic illustration of the disassembly process of a cluster of nanocatalysts into lots of small clusters along with the increase of the coverage area of the nanocatalysts. (b) Successive images of the disassembly process of a cluster of nanocatalysts.

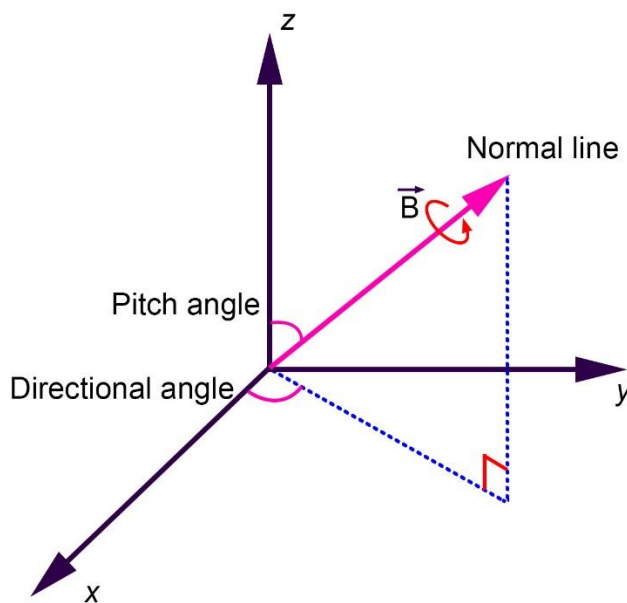


Figure S8 Schematic showing the pitch angle and directional angle of Helmholtz coil generated magnetic field, Related to Figure 5.

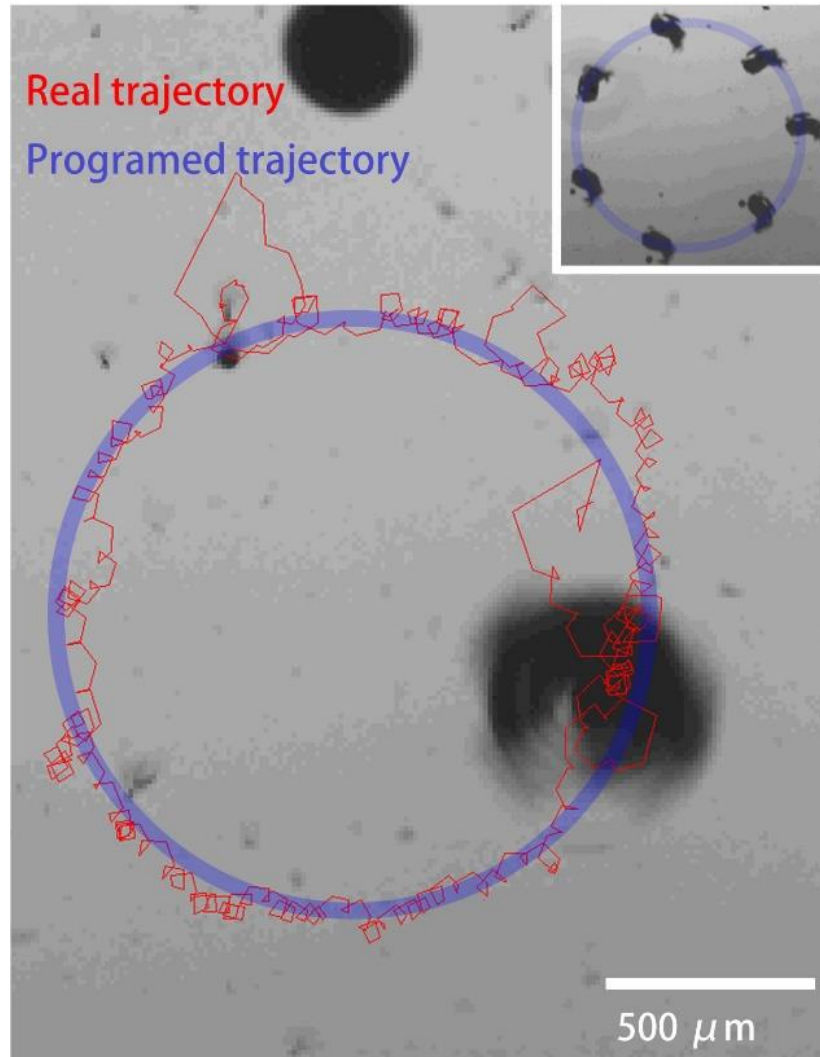


Figure S9 Locomotion of the B-MCS with programed trajectory, Related to Figure 5. The round circle with semitransparent blue color is the programed trajectory and the red line is the real motion trail tracked with the computer. The real trail matches well with the programed trajectory, with slight disturbance cause by the surroundings.

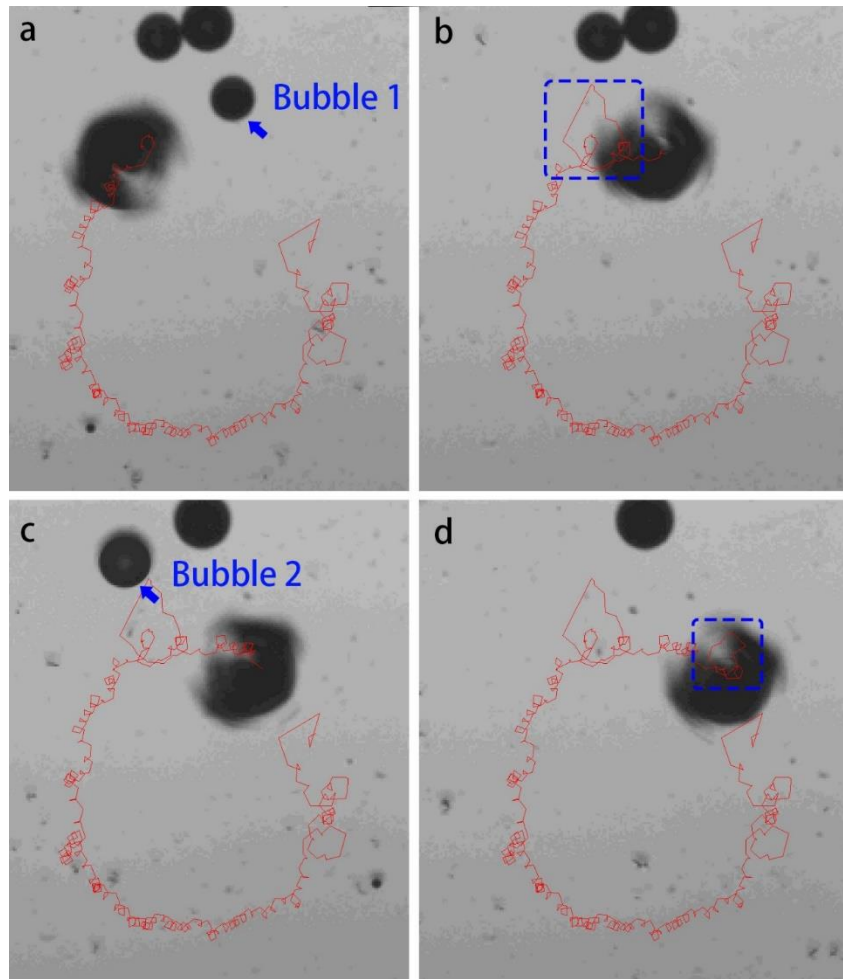


Figure S10 Disturbance of the locomotion trail of the B-MCS by the generated bubbles, Related to Figure 5. The navigating B-MCS cut the bubbles around their trajectory. On the contrary, the bubbles show some disturbance to the locomotion trail of the B-MCS.

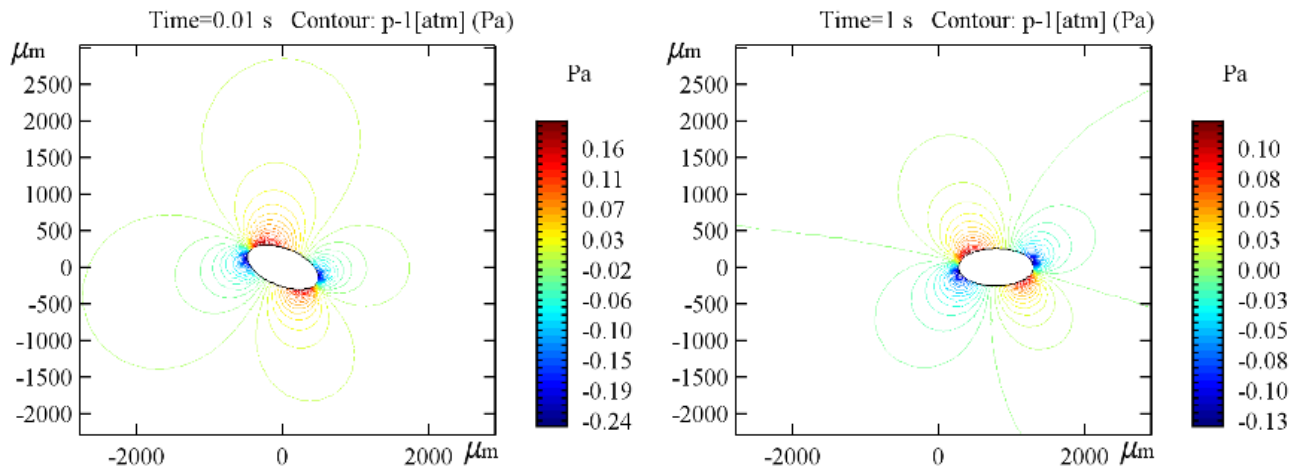


Figure S11 Simulation results of the pressure field of B-MCS with translational motion, Related to Figure 5. For the B-MCS, local fluid environment introduces pressure difference around surface of swarm. Analyzing an elliptical structure, the front sides facing rotating direction (clockwise shown in Figures) generates higher pressure. Difference of pressure helps create bubbles from catalytic reaction.

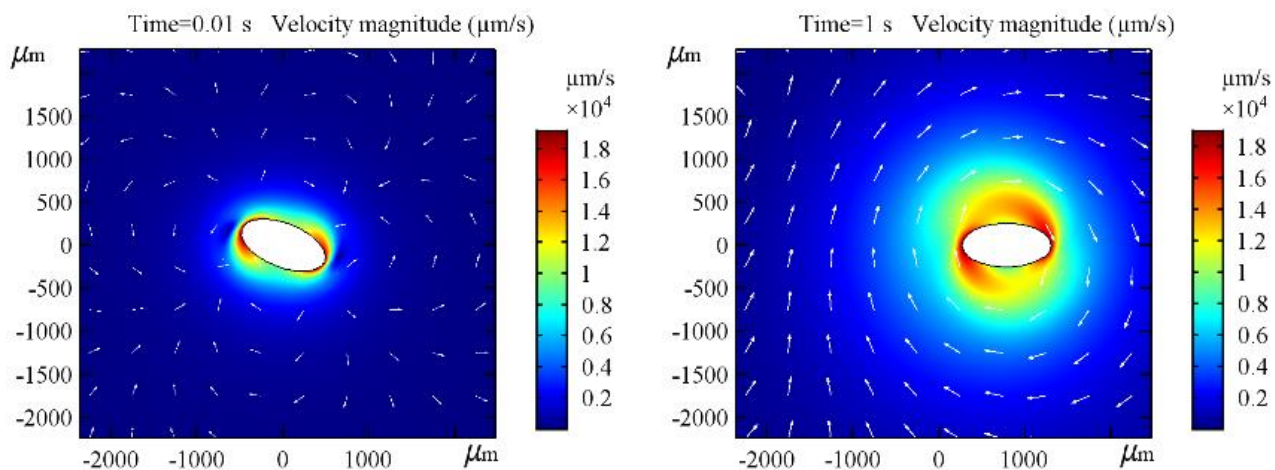


Figure S12 Simulation results of the flow field of B-MCS with translational motion, Related to Figure 5. The velocity field generated from translational and rotational movement decides interaction among swarms, obstacles and boundary conditions. The state of flow environment with B-MCS is shown in the figure by calculating the interaction between fluid and structure and equation $\rho \frac{D\vec{v}}{Dt} = \vec{F} + \nabla \cdot (-p\vec{I} + \mu(\nabla\vec{v} + (\nabla\vec{v})^T))$ (Ji et al., 2018). The stronger velocity and shear stress appear at the long axis of the swarm.

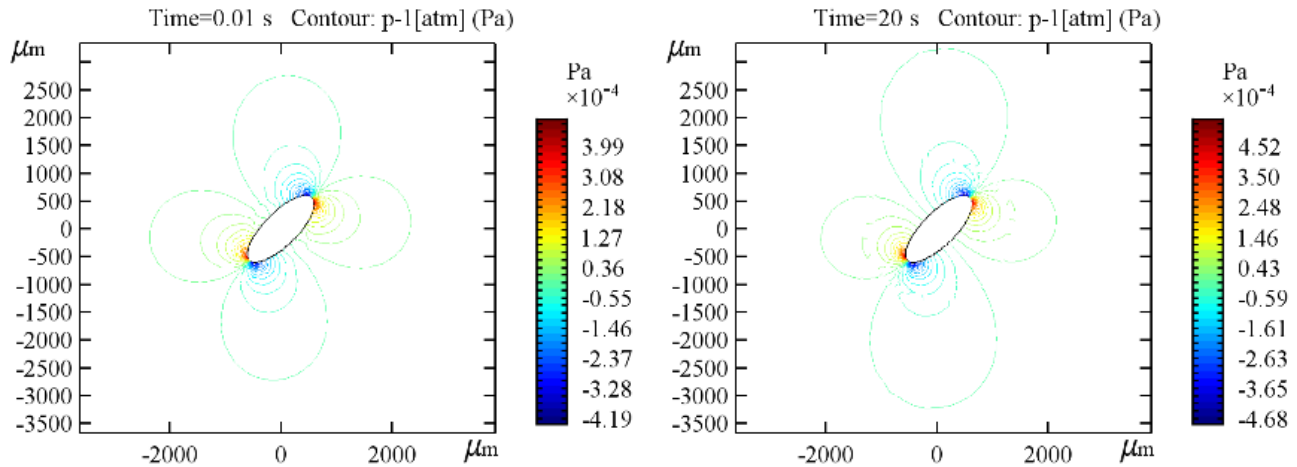


Figure S13 Simulation results of the pressure field of MCS with translational motion, Related to Figure 5. Comparing to small particle swarms split by bubbles, a big pile of particle swarm has low response rate particle swarms of small fractions rotate along the surface continuously. Therefore, low pressure and velocity field come out in such condition.

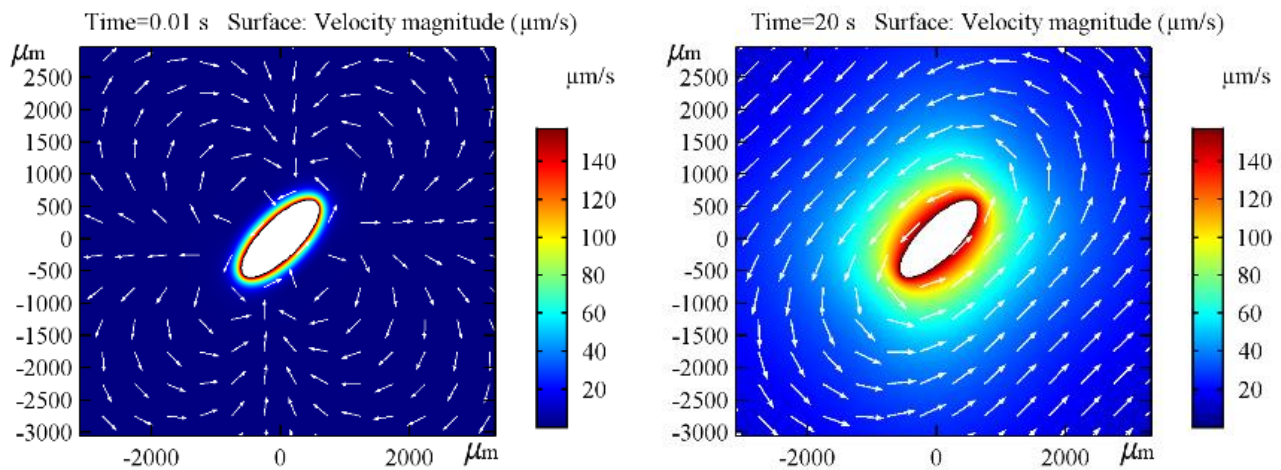


Figure S14 Simulation results of the flow field of MCS with translational motion, Related to Figure 5. As for the rotating fractions, their rotating velocity and tangential velocity is approximate the same, otherwise the whole pile of swarm collapses. Thus the surrounding fluid velocity is about the same, which is significantly smaller than B-MCS case.

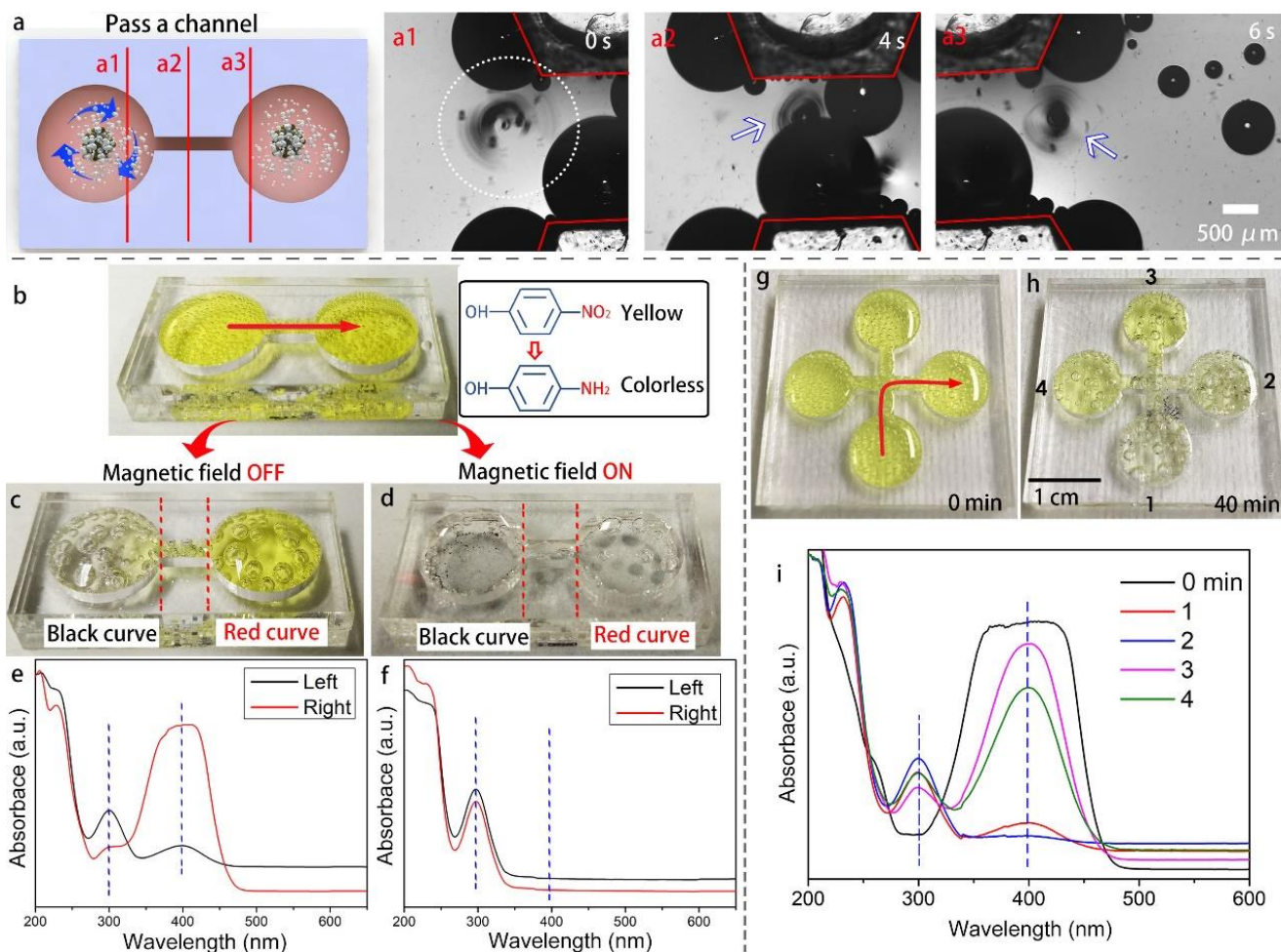


Figure S15. Spatial enhancement of the catalytic activity, Related to Figure 2. (a) Schematic illustration and successive images of the locomotion of the gathering nanocatalysts passing through a channel in the solution of 4-NP and NaBH₄ under a rotating magnetic field. Therein, a1, a2 and a3 represent the original, intermediate and final sites respectively. (b) Schematic illustration of the B-MCS motion of the nanocatalysts for targeted catalysis and optical image shows the 4-NP and NaBH₄ solution in the channel with two reservoirs. (c) Optical image shows the 4-NP and NaBH₄ solution in the channel after 30 min of catalysis by the nanocatalysts without swarming motion. The 4-NP in the left channel are largely catalyzed to a quite low level whereas the concentration of unreacted 4-NP in the right channel are still high, approximately 3 times of the left channel. (d) Optical image shows the 4-NP and NaBH₄ solution in the channel after 30 min of catalysis by the nanocatalysts with B-MCS motion. (e) and (f)

show the UV-vis spectra the catalytic solutions at 30 min by the nanocomposite without and with B-MCS motion, respectively. The magnetic field strength is 6 mT, the frequency is 6 Hz and the pitch angle is 2° . (g) Optical image shows the 4-NP and NaBH₄ solution in the channel with four reservoirs. (h) Optical image shows the color change of the solution in the channel after 40 min of catalysis by the nanocatalysts with B-MCS motion to the targeted location indicated by the red line. (i) UV-vis spectra of the original solution (0 min) and the solutions inside the reservoirs 1-4 at the time-point of 40 min with B-MCS, the conversions of the 4-NP are calculated to be 78%, 83%, 8% and 25% in the Reservoir 1-4, respectively, denoting the controllable selectively of catalysis in space by the proposed B-MCS.

Supplemental References

Choi, C. K. K., Zhuo, X., Chiu, Y. T. E., Yang, H. R., Wang, J. F., and Choi, C. H. J. (2017). Polydopamine-based concentric nanoshells with programmable architectures and plasmonic properties. *Nanoscale*, *9*, 16968-16980.

Deng, H., Li, X. L., Peng, Q., Wang, X., Chen, J. P., and Li, Y. D. (2005). Monodisperse magnetic single-crystal ferrite microspheres. *Angew. Chem. Int. Ed.* *44*, 2782-2785.

Jana, N. R., Gearheart, L., and Murphy, C. J. (2001). Wet Chemical Synthesis of High Aspect Ratio Cylindrical Gold Nanorods. *J. Phys. Chem. B.*, *105*, 4065-4067.

Ji, F., Zhou, D., Zhang, G., and Li, L. (2018). Numerical Analysis of Visible Light Driven Gold/Ferric Oxide Nanomotors. *IEEE Transactions on Nanotechnology* *17*, 692-696.